

# Quantum phase transition and composite excitations of antiferromagnetic spin trimer chains in a magnetic field

Jun-Qing Cheng,<sup>1,2,3</sup> Zhi-Yao Ning,<sup>1</sup> Han-Qing Wu,<sup>1,\*</sup> and Dao-Xin Yao<sup>1,†</sup>

<sup>1</sup>*State Key Laboratory of Optoelectronic Materials and Technologies, Center for Neutron Science and Technology, Guangdong Provincial Key Laboratory of Magnetoelectric Physics and Devices, School of Physics, Sun Yat-Sen University, Guangzhou 510275, China*

<sup>2</sup>*School of Physical Sciences, Great Bay University, 523000, Dongguan, China*

<sup>3</sup>*Great Bay Institute for Advanced Study, Dongguan 523000, China*

(Dated: November 22, 2024)

Motivated by recent advancements in theoretical and experimental studies of the high-energy excitations on an antiferromagnetic trimer chain, we numerically investigate the quantum phase transition and composite dynamics in this system by applying a magnetic field. The numerical methods we used include the exact diagonalization, density matrix renormalization group, time-dependent variational principle, and cluster perturbation theory. From calculating the entanglement entropy, we have revealed the phase diagram which includes the XY-I, 1/3 magnetization plateau, XY-II, and ferromagnetic phases. Both the critical XY-I and XY-II phases are characterized by the conformal field theory with a central charge  $c \simeq 1$ . By analyzing the dynamic spin structure factor, we elucidate the distinct features of spin dynamics across different phases. In the regime with weak intertrimer interaction, we identify the intermediate-energy and high-energy modes in the XY-I and 1/3 magnetization plateau phases as internal trimer excitations, corresponding to the propagating of doublons and quartons, respectively. Notably, applying a magnetic field splits the high-energy spectrum into two branches, labeled as the upper quarton and lower quarton. Furthermore, we explore the spin dynamics of a frustrated trimerized model closely related to the quantum magnet  $\text{Na}_2\text{Cu}_3\text{Ge}_4\text{O}_{12}$ . In the end, we extend our discuss on the possibility of the quarton Bose-Einstein condensation in the trimer systems. Our results are expected to be further verified through the inelastic neutron scattering and resonant inelastic X-ray scattering, and also provide valuable insights for exploring high-energy exotic excitations.

## I. INTRODUCTION

Understanding the profound physical nature of the strongly correlated many-body systems is a challenging and fascinating task in modern condensed-matter physics. Among the various physical properties, magnetic excitation plays a crucial role in understanding the magnetic structures of quantum materials and can be studied both theoretically and experimentally [1–22]. In particular, the strong quantum fluctuations in low-dimensional systems give rise to a variety of exotic ground states and excitations, such as the Luttinger liquid and spinon excitation, which have attracted significant interest [1–12]. Quasi one-dimensional (1D) magnetic materials can be effectively described by the Heisenberg spin chain, and its various extensions have been extensively investigated. For example, the gapless two-spinon continuum [2] has been observed through inelastic neutron scattering in quasi 1D material  $\text{KCuF}_3$  [3, 4] and the frustrated ferromagnetic spin-1/2 chain compound  $\text{LiCuVO}_4$  [5]. Multi-spin excitations can be detected using the resonant inelastic X-ray scattering (RIXS) technique in the material  $\text{Sr}_2\text{CuO}_3$  [6, 7]. Furthermore, the high-energy string excitations have been proposed as the dominant excitations in the isotropic Heisenberg antiferromagnet

based on the Bethe ansatz [8], and have recently been observed in an antiferromagnetic Heisenberg–Ising chain compounds  $\text{SrCo}_2\text{V}_2\text{O}_8$  and  $\text{BaCo}_2\text{V}_2\text{O}_8$  under strong longitudinal magnetic fields using the high-resolution terahertz spectroscopy [9, 10].

Besides the uniform spin chains, quantum materials often exhibit structures that consist of more than one spin per unit cell, resulting in more rich magnetic properties. Among that, ladder systems are well-studied examples of quasi-1D systems with more spins in a unit cell, where the gapless or gapped excitation spectrum depends on whether the rungs contain an odd or even number of  $S = 1/2$  spins, respectively [23]. This behavior is analogous to the Haldane’s conjecture regarding spin chains with half-odd-integer or integer spins [24]. Among the experimental realizations, the two-leg ladder compound  $(\text{C}_7\text{H}_{10}\text{N})_2\text{CuBr}_4$  is noteworthy due to the excellent agreement between its inelastic neutron scattering spectrum and the dynamic spin structure factor derived from the model calculations [25]. Besides the ladder spin system, spatial inhomogeneous is another way to enlarge the unit cell with more spins. For instance, the model featuring two-spin unit cells with alternating couplings  $J_1 - J_2$ , called alternating or dimerized Heisenberg chain, has been well studied. A gap appears in the spectrum if  $J_1 \neq J_2$ , as this modulation causes the spinons of the uniform Heisenberg antiferromagnetic chain ( $J_1 = J_2$ ) to be confined into triplons that can be considered as weakly bound of spinons when

\* wuhanq3@mail.sysu.edu.cn

† yaodaoy@mail.sysu.edu.cn

$J_2 \approx J_1$  [26]. Extended to trimerized system with three-spin unit cells and repeated couplings  $J_1 - J_1 - J_2$ , the so-called trimerized Heisenberg chain is less studied and would exhibit very different magnetic excitations due to odd number of spins in a unit cell [11]. Moreover, this trimerized structure has been observed in real materials like  $A_3Cu_3(PO_4)_4$  ( $A=Ca, Sr, Pb$ ) [27–32],  $(C_5H_{11}NO_2)_2 \cdot 3CuCl_2 \cdot 2H_2O$  [33], and  $Ba_4Ir_3O_{10}$  [34, 35]. In the iridate  $Ba_4Ir_3O_{10}$ , where three-spin unit cells form layered trimers, fractional spinon excitation has been observed in the RIXS experiments [34, 35].

In our previous work [11], we have investigated the spin dynamics of trimer chain characterized by repeated couplings  $J_1 - J_1 - J_2$ , whereas the intratrimer  $J_1$  is larger than intertrimer  $J_2$ . Our findings show that the low-energy excitation corresponds to the two-spinon continuum can be well described by the uniform Heisenberg model of effective trimer block spins [11]. Most interestingly, some new composite excitations of the novel quasiparticles, known as doublons and quartons, have been predicted in the intermediate-energy and high-energy spectra, respectively, and have been subsequently confirmed in the inelastic neutron scattering measurements on  $Na_2Cu_3Ge_4O_{12}$  [12]. As  $J_2/J_1 \rightarrow 1$ , the doublons and quartons lose their identities and fractionalize into the conventional two-spinon continuum. We have also extended the doublon and quarton excitations to 2D trimer systems [22]. Even though we have a clear understanding these exotic excitations, how to control these excitations using magnetic field is still an interesting topic.

In this paper, we want to study the effect of magnetic field on the doublons and quartons in the trimer chain illustrated in Fig. 1(a). To achieve this, we employ various techniques, including exact diagonalization (ED), density matrix renormalization group (DMRG) [36–38], time-dependent variational principle (TDVP) [39, 40], and cluster perturbation theory (CPT) [41–44] to investigate the excitation spectra of trimer chain under the magnetic field. By mapping the entanglement entropy onto the parameter space, we identify the XY-I, the 1/3 magnetization plateau, the XY-II and the ferromagnetic phases. In the gapless XY-I and XY-II phases, both central charges  $c \simeq 1$  indicate that these two phases are well described by the conformal field theory. More importantly, we investigate the intermediate-energy and high-energy excitations for small  $g$  in the XY-I and 1/3 magnetization plateau phases. Our analysis demonstrates that the intermediate-energy and high-energy modes are primarily governed by the internal trimer excitations, referred to as the doublons and quartons, respectively. Furthermore, these features of the excitation spectra can also be observed in the spin chain with a trimer structure that is closely associated with the quantum magnet  $Na_2Cu_3Ge_4O_{12}$  [12]. The magnetic field drives the lower quarton toward zero energy, suggesting the potential for observing the magnetic-field-induced quarton Bose-Einstein condensation (BEC) in the quantum magnet  $Na_2Cu_3Ge_4O_{12}$ . Our results may facilitate further

exploration of the high-energy spin excitation mechanisms in other systems containing clusters with odd spins.

## II. RESULTS

### A. Model

The Hamiltonian of the spin-1/2 antiferromagnetic trimer chain subjected to a longitudinal magnetic field reads

$$\mathcal{H} = \sum_{i=1}^N [J_1 (\mathbf{S}_{i,a} \cdot \mathbf{S}_{i,b} + \mathbf{S}_{i,b} \cdot \mathbf{S}_{i,c}) + J_2 \mathbf{S}_{i,c} \cdot \mathbf{S}_{i+1,a}] - H_z \sum_{j=1}^{3N} S_j^z, \quad (1)$$

where  $\mathbf{S}_{i,\gamma}$  is the spin-1/2 operator at the  $\gamma$ -th sublattice site of the  $i$ -th trimer, the intratrimer labels  $\gamma \in \{a, b, c\}$  are explained in Fig. 1(a).  $H_z$  represents the strength of external magnetic field, which breaks the SU(2) symmetry. The system comprises a total of  $N$  trimers, resulting in a system length of  $L = 3N$ . The tuning parameter  $g$  is defined as  $g = J_2/J_1$ . For simplicity, we set the intratrimer interaction  $J_1 = 1$  as the energy unit, so that intertrimer interaction  $J_2 = g$ . Our interest is in the range of coupling ratios  $g \in [0, 1]$ , where the system evolves between the isolated trimers and the isotropic Heisenberg antiferromagnetic chain.

### B. Quantum phase transition

In the absence of a magnetic field, the antiferromagnetic quantum spin trimer chain exhibits a gapless low-energy excitation known as the two-spinon continuum [11]. When a magnetic field is applied, the SU(2) symmetry is broken, leading to the emergence of a quantum phase transition driven by the competition between the interaction and magnetic field. In this subsection, we aim to investigate the detailed phase diagram using the DMRG method.

Quantum entanglement provides a distinctive framework for unveiling the ground-state properties of many-body systems and has been extensively used to study the quantum phase transitions [45–50]. Entanglement entropy, a crucial metric for assessing bipartite quantum entanglement, can be easily derived from DMRG calculations. Its definition is given by

$$S = -\text{Tr} [\rho_A \ln \rho_A], \quad (2)$$

where the reduced density matrix  $\rho_A$  is the partial trace of the density matrix of the whole system  $\rho$ ,  $\rho_A = \text{Tr}_B [\rho]$ . If A and B are entangled, the reduced density matrix must be a mixed state, and the entanglement entropy

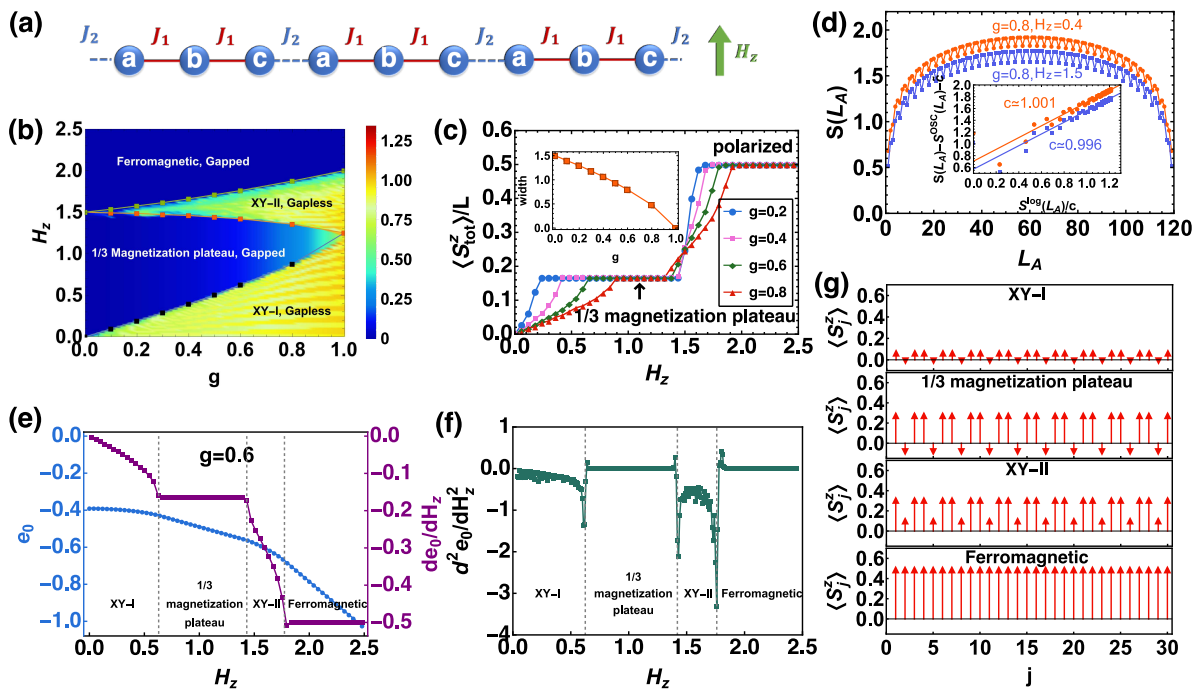


FIG. 1. **Quantum phase transitions.** (a) Schematic representation of a trimer spin chain subjected to a longitudinal magnetic field. The analysis focuses on systems characterized by the condition  $J_1 \geq J_2 > 0$ , with the letters  $a, b, c$  denoting the three spins within a unit cell. (b) The phase diagram is obtained by employing the DMRG method to map the entanglement entropy onto the parameter space  $(g, H_z)$  for a system with  $L = 180$  spins. (c) Magnetization curves are illustrated as a function of  $H_z$  for different  $g$  in a system with  $L = 180$ . Inset shows the width of 1/3 magnetization plateau as a function of  $g$ . (d) Entanglement entropy  $S(L_A)$  as a function of the subsystem size  $L_A$  under open boundary conditions. Solid lines in the inset represent the best fits to the CFT scaling form, with the optimal values for the central charges provided. (e) Ground state energy of per spin  $e_0 = E_0/L$  and its first derivative  $de_0/dH_z$  as a function of  $H_z$  for the system with  $L = 210$ . (f) The second derivative  $d^2e_0/dH_z^2$  as a function of  $H_z$  for the system with  $L = 210$ . (g) Magnetization of each spin obtained by DMRG for four distinct phases where  $g = 0.6$  and  $H_z = 0.3, 1.0, 1.5, 2.0$ .

quantifies the degree of this mixing. By effectively analyzing the entanglement entropy, the characteristics of ground states in various quantum phases can be extracted. Therefore, the entanglement entropy serves as a viable and useful tool for investigating the quantum phase transitions. As illustrated in Fig. 1(b), the entanglement entropy reveals four distinct phases within the  $(g, H_z)$  parameter space. When an external magnetic field is applied, a transition from the Néel phase to an incommensurate phase occurs, propelling the system into the XY-I phase. However, the magnetic field is insufficient to open a gap, resulting in a ground state that remains gapless with a nonzero entanglement entropy. In Fig. 1(c), the magnetization increases with the magnetic field in the XY-I phase until a fractional magnetization plateau is reached.

The fractional magnetization plateau observed in the magnetization curves can be understood through the Oshikawa-Yamanaka-Affleck (OYA) criterion [51]:

$$n(s - m) = \text{integer} \quad (3)$$

where  $n$  is the number of spins in a unit cell,  $m$  is the magnetization per site and  $s$  denotes the magnitude of

spin. For the trimer chain, it has  $n = 3$ ,  $s = 1/2$ , so when  $n(s - m) = 0$  it results in  $m = 1/2$ , which corresponds to the full polarized state. Conversely, when  $n(s - m) = 1$  it yields  $m = 1/6$  corresponding to the 1/3 magnetization plateau. Fig. 1(c) clearly illustrates the existence of these two plateaus. In the 1/3 magnetization plateau phase, the external magnetic field is insufficient to decouple the singlets. As  $g$  increases, the width of magnetization plateau decreases, ultimately vanishing at  $g = 1$  where the trimer chain transitions into the uniform Heisenberg chain. From the magnetization of each spin, as shown in Fig. 1(g), we can observe that the magnetization exhibits a periodic pattern corresponding to the trimerized structure. Specifically, the magnetization of the central spin in each trimer increases as  $H_z$  rises. Importantly, the magnetization of each spin remains fixed even as the magnetic field increases in the 1/3 magnetization plateau phase. The ground state of an isolated trimer in the presence of a magnetic field is described by,

$$|0\rangle = \frac{1}{\sqrt{6}} (|\uparrow\uparrow\downarrow\rangle - 2|\uparrow\downarrow\uparrow\rangle + |\downarrow\uparrow\uparrow\rangle), \quad (4)$$

which is also the antiferromagnetic trimer state of the Haldane plateau observed in one-dimensional  $(S, s) =$

(1, 1/2) mixed spin chain [52]. In the 1/3 magnetization plateau phase, as shown in Fig. 1(g), the expectation values of the  $z$  components of three spins, labeled  $a, b, c$ , are 0.322,  $-0.144$ , and 0.322, respectively. These values are approximately coincide with the ideal state, which has expectation values of  $1/3$ ,  $-1/6$ , and  $1/3$ . This indicates that the 1/3 magnetization plateau state exhibits Néel order along the direction of magnetic field, with each trimer effectively possessing a spin of  $1/2$ , thereby creating the appearance of polarization for each trimer.

As the magnetic field increases, the singlets are disrupted, resulting in to the emergence of the XY-II phase. The system remains gapless, exhibiting a nonzero entanglement entropy in the ground state. Additionally, the average magnetization is greater than that in the XY-I phase and increases with the magnetic field. As long as the magnetic field is sufficiently strong, all spins become polarized, leading to the formation of an additional magnetization plateau and the emergence of a ferromagnetic phase. We also utilize the properties of entanglement to suggest a potential conformal field theory description of the gapless phases. The Rényi entanglement entropy of subsystem  $A$  is defined as follows:

$$S_\nu(\rho_A) = \frac{1}{1-\nu} \ln(\text{Tr}\{\rho_A^\nu\}). \quad (5)$$

In the limit  $\nu \rightarrow 1$ , the above expression simplifies to the von Neumann entanglement entropy,

$$S(\rho_A) = \lim_{\nu \rightarrow 1} S_\nu(\rho_A) = -\text{Tr}[\rho_A \ln \rho_A]. \quad (6)$$

The Rényi entanglement entropy of subsystem  $A$  follows the scaling form [53–55]:

$$S_\nu(L_A) = S_\nu^{\text{log}}(L_A) + S_\nu^{\text{osc}}(L_A) + \tilde{c}_\nu, \quad (7)$$

where

$$S_\nu^{\text{log}}(L_A) = \frac{c}{6\eta} \left(1 + \frac{1}{\nu}\right) \ln \left\{ \left[ \frac{\eta L}{\pi} \sin \left( \frac{\pi L_A}{L} \right) \right] \right\}, \quad (8)$$

and

$$S_\nu^{\text{osc}}(L_A) = F_\nu \left( \frac{L_A}{L} \right) \frac{\cos(2k_F L_A)}{\left| \frac{2\eta L}{\pi} \sin(\pi L_A/L) \right|^{\frac{2\Delta_1}{\eta\nu}}}. \quad (9)$$

Here,  $\eta = 1, 2$  corresponds to periodic and open boundary conditions, respectively. The central charge  $c$ , the Fermi momentum  $k_F$ , and the scaling dimension  $\Delta_1$  are universal parameters.  $F_\nu(L_A/L)$  is a universal scaling function and  $\tilde{c}_\nu$  is a nonuniversal constant. By fitting the DMRG data with these functions for  $\nu = 1$ , we extract the central charges of the two XY phases, which serve as indicators of their universality classes. As shown in Fig. 1(d), the both XY phases are described by the conformal field theory with central charges  $c \simeq 1$ .

Furthermore, to identify the types of quantum phase transitions present, we have conducted an analysis involving the computation of the first and second derivatives of the ground state energy with respect to the magnetic field  $H_z$ , see Figs. 1(e) and 1(f). According to the

Hellmann-Feynman theorem, the magnetization curves (see Fig.1(c)) and the first derivative of the ground state energy  $de_0/dH_z$  exhibit the similar behaviors, characterized by continuity but a lack of differentiability near the critical points. The second derivative  $d^2e_0/dH_z^2$  displays nonanalytic behavior in the vicinity of these critical points. Collectively, these results suggest that the quantum phase transitions between the XY-I, 1/3 magnetization plateau, XY-II, and ferromagnetic phases are second-order quantum phase transitions. In Supplementary note 1, we also provide the real-space spin-spin correlation function for the four phases. The correlation functions in the XY-I and XY-II phases decay according to power laws, with the critical exponents converging towards 1, which is analogous to the  $S = 1/2$  isotropic Heisenberg chain [56].

### C. Excitation spectra

In this section, we present the spin excitation spectra of the trimer chain in an external magnetic field, utilizing the dynamical structure factor (DSF):

$$S^{\alpha\beta}(q, \omega) = \sum_j e^{-iqj} \left[ \int_{-\infty}^{\infty} dt e^{i\omega t} \langle \hat{S}_j^\alpha(t) \hat{S}_0^\beta \rangle \right], \quad (10)$$

where  $\alpha, \beta$  refer to the spin components  $x, y$ , and  $z$ . We calculated the DSF using the CPT and DMRG-TDVP methods to study the spin dynamics under the modification of control parameters,  $g$  and  $H_z$ . Detailed calculations can be found in Sec. IV. In our previous study, we have utilized the quantum Monte Carlo methods with subsequent numerical analytic continuation to investigate the spin dynamics of trimer chain in the absence of magnetic field, revealing the doublons and quartons in the intermediate-energy and high-energy regimes, respectively [11]. For comparison, the spectral characteristics are also assessed using the DMRG-TDVP and CPT calculations, with results available in Supplementary note 2. Furthermore, we provide the spin excitation spectra obtained from ED calculation in Supplementary note 5.

In Fig. 2, the transverse excitation spectra  $S^{xx}(q, \omega)$  for four distinct phases are presented. The excitations are gapless in two XY phases and gapped in the 1/3 magnetic plateau and ferromagnetic phases. To understand the spin dynamics of the XY-I and XY-II phases, we will examine the zero-energy excitations. The incommensurability observed in the spin dynamics of an AF spin-1/2 chain subjected to a longitudinal magnetic field can be interpreted using the language of spinless fermions [57]. The longitudinal magnetic field acts as a chemical potential, which alters the band filling and breaks the degeneracy of the electron-hole bands. The intraband and interband zero-energy excitations correspond to the longitudinal and transverse fluctuations, respectively. For the trimer chain subjected to a longitudinal magnetic field, incommensurability arises from the splitting of the

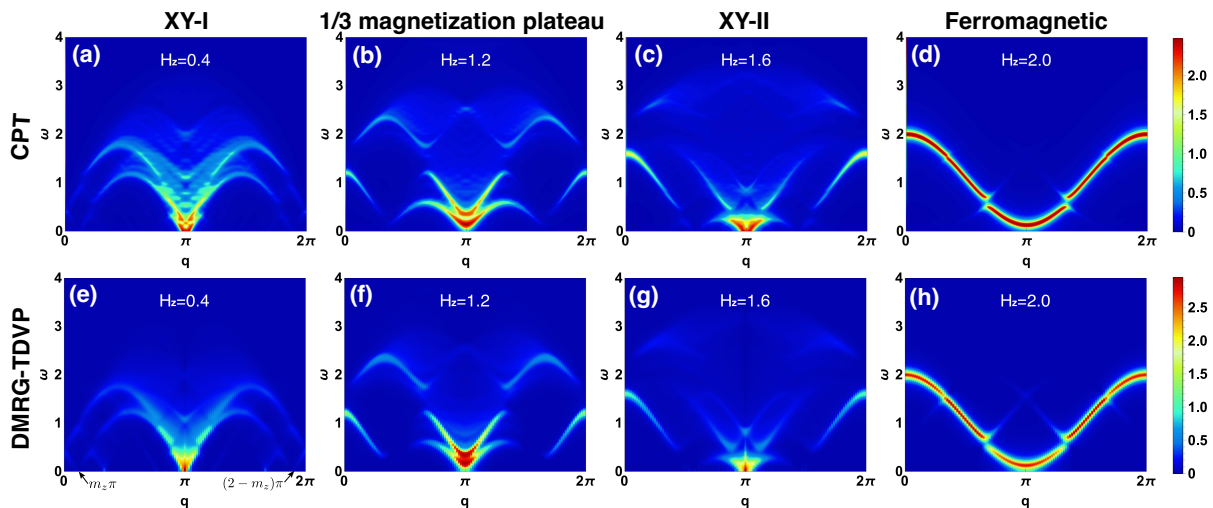


FIG. 2.  $S^{xx}(q, \omega)$  obtained from CPT and DMRG-TDVP calculations for different phases.  $S^{xx}(q, \omega)$  in (a)(e) XY-I phase, (b)(f) 1/3 magnetization plateau phase, (c)(g) XY-II phase, and (d)(h) Ferromagnetic phase. All results are derived from the case where  $g = 0.8$ , and the DMRG-TDVP calculations are conducted for a system with length  $L = 120$ . The color coding of  $S^{xx}(q, \omega)$  uses a piecewise function with the boundary value  $U_0 = 2$ . Below this boundary, the low-intensity portion is characterized by a linear mapping of the spectral function to the color bar, while above the boundary a logarithmic scale is used,  $U = U_0 + \log_{10}[S^{zz}(q, \omega)] - \log_{10}(U_0)$ .

bands. Figs. 2(a)(e) display the transverse excitations  $S^{xx}(q, \omega)$  as the number of particles is varied, leading to fluctuations that reach zero energy at incommensurate wave numbers  $q = m_z\pi$  and  $q = (2 - m_z)\pi$  in addition to  $q = \pi$ . The spectral weight is concentrated at the commensurate positions corresponding to each reciprocal lattice points at  $q = \pi$  in the XY-I and XY-II phases. In the high-energy regime, a continuum is observed in both the 1/3 magnetization plateau and the XY-II phases. At the ferromagnetic phase, see Figs. 2(d)(h), all spins are polarized, and the spin excitation continues to propagate as magnons. Energy gaps are observed at the edges of the Brillouin zone, specifically at  $q = \pi/3, 2\pi/3, 4\pi/3, 5\pi/3$  where spin waves are diffracted due to the periodic potential of the trimerized interaction. Consequently, the magnons at the edges of the Brillouin zone exhibit two distinct energy levels for the same wave vector. In Supplementary note 3, we also present the longitudinal excitation spectrum and discuss the zero-energy excitations that correspond to the longitudinal fluctuations.

In our previous study [11], we found that a smaller  $g$  induces rich intermediate-energy and high-energy excitations beyond the spin wave. Therefore, it is of great interest to investigate the evolution of intermediate-energy and high-energy quasiparticles, referred to as the doublons and quartons, under the influence of a magnetic field. In this study, we focus on the weak intertrimer coupling  $g = 0.3$  to examine their dynamical evolutions. In this case, the system behaves as isolated trimers, allowing for straightforward analysis. From Figs. 3(a)(e), we observe that the low-energy excitation resembles the excitation spectrum of conventional spinons in a magnetic field. A splitting of the dispersion relation occurs,

characterized by the emergent fermions of the Heisenberg chain in the presence of magnetic field [58]. The intermediate-energy spectrum shows minimal separation near  $q = \pi/3$  and  $q = 5\pi/3$ , with a continuum emerges, possibly due to the propagation of doublons dressed by spinons [11]. The high-energy spectrum is distinctly split into two branches by the magnetic field.

As  $H_z$  increases, see Figs. 3(b)(f), the excitation gap opens, leading the system into a 1/3 magnetization plateau phase. Consequently, the lower spectrum of high-energy excitations with  $\Delta M = 1$  transitions to the low-energy regime. When  $H_z = 1.5$ , the system evolves into the gapless XY-II phase (see Figs. 3(c)(g)), where the low-energy, intermediate-energy and high-energy spectra exhibit clear differentiation. In the ferromagnetic phase  $H_z = 2.0$ , shown in Figs. 3(d)(h), the spin excitation are predominantly characterized by spin waves due to complete spin polarization. Additionally, some energy gaps are observed at the Brillouin zone edges  $q = \pi/3, 2\pi/3, 4\pi/3, 5\pi/3$ , which is consistent with the results of Figs. 2(d)(h).

The preceding discourse primarily focuses on the impact of a magnetic field on the spin excitation spectra of a trimer chain with a constant intertrimer interaction strength. To enhance our understanding of the spin dynamics within such a trimer chain under the influence of a magnetic field, we present additional results obtained through DMRG-TDVP calculations for varying values of the  $g$  parameter. Further details are provided in Supplementary Note 4 for clarification.

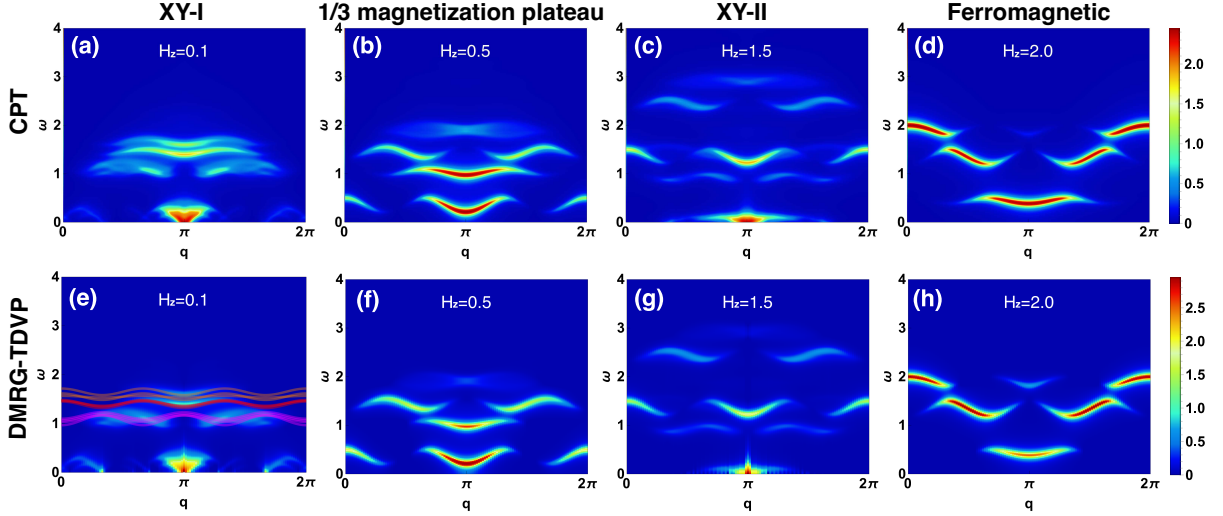


FIG. 3.  $\mathcal{S}^{xx}(q, \omega)$  obtained from CPT and DMRG-TDVP calculations for weak intertrimer interaction.  $\mathcal{S}^{xx}(q, \omega)$  in (a)(e) XY-I phase, (b)(f) 1/3 magnetization plateau phase, (c)(g) XY-II phase, and (d)(h) Ferromagnetic phase. All results are derived from the case where  $g = 0.3$ , and the DMRG-TDVP calculations are conducted for a system with length  $L = 120$ . The color coding of  $\mathcal{S}^{xx}(q, \omega)$  uses a piecewise function with the boundary value  $U_0 = 2$ .

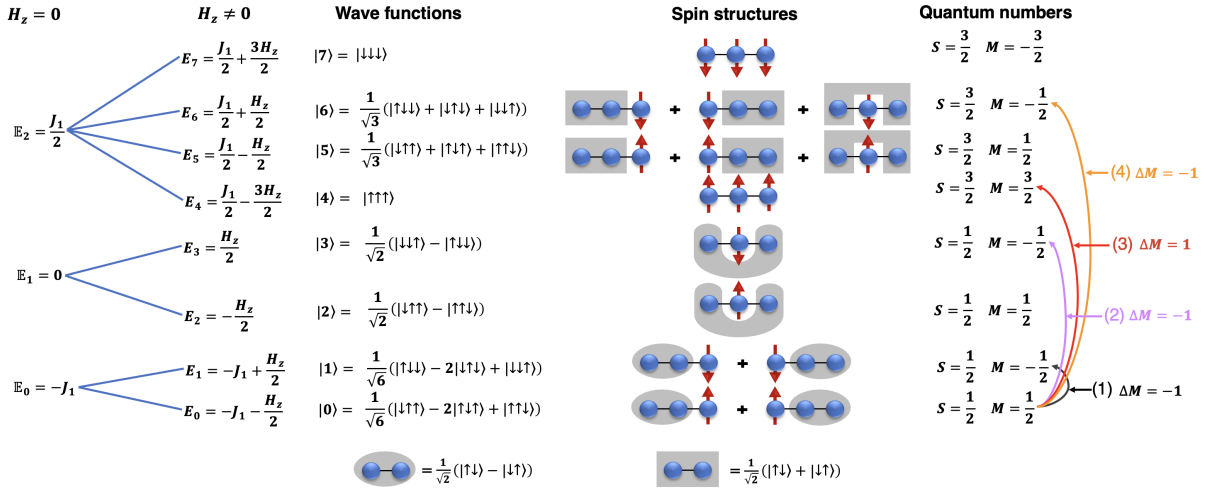


FIG. 4. The level spectrum, wave functions, and quantum numbers of one isolated trimer under a longitudinal magnetic field. The second column lists the wave functions in the spin- $z$  basis, while the third column presents the spin structures using a basis of singlets (gray ovals and rounded shapes), zero-magnetization triplets (gray square shapes), and unpaired spins (arrows). The last column lists the total spin quantum number  $S$ , magnetic quantum number  $M$ , and the internal trimer excitations with  $\Delta M = \pm 1$ .

#### D. Excitations mechanisms

To gain a deeper understanding of the intermediate-energy and high-energy spin dynamics, it is instructive to analyze the complete level spectrum and the corresponding eigenvectors of a single trimer. As depicted in Fig. 4, the application of a magnetic field causes the splitting of three energy levels into eight distinct levels. Notably, the eigenvectors, spin quantum numbers, and magnetic quantum numbers remain invariant. When  $H_z \leq 1.5$ ,

the ground state of the trimer is denoted as  $|0\rangle$  with an energy  $E_0 = -J_1 - H_z/2$ . Considering the excitations with  $|\Delta M| = 1$  from  $|0\rangle$ , only four cases satisfy this condition, as indicated in the last column of Fig. 4. For small  $g$ , the coupling between trimers can be treated as a perturbation of the product state of isolated trimers. This approach has been validated in our previous study of a trimer chain without an external magnetic field [11]. Here, the perturbative analysis remains an effective tool to handle with the spin excitations of trimer chain under a magnetic field, particularly in the XY-I and 1/3 magne-

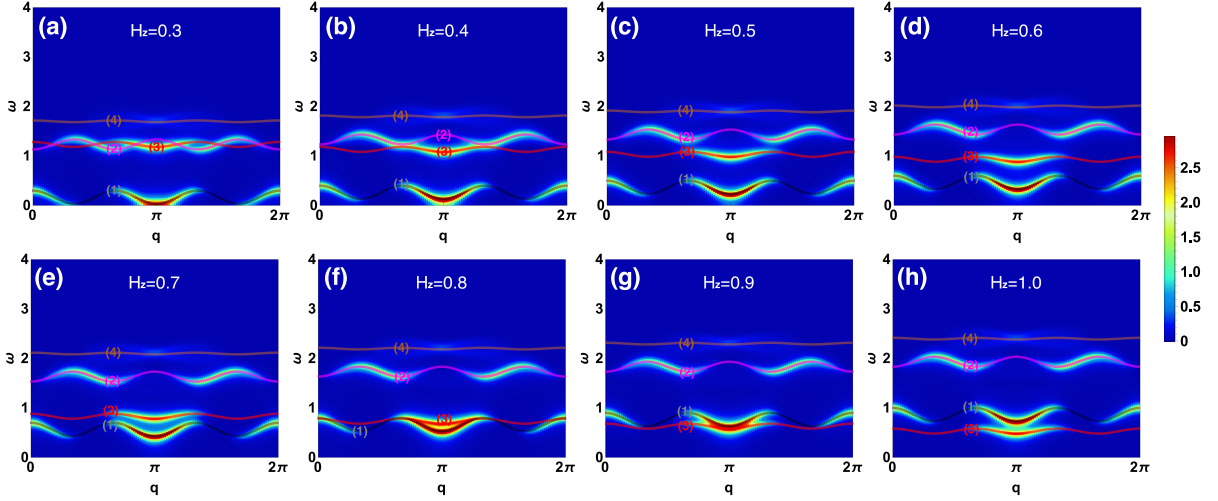


FIG. 5.  $\mathcal{S}^{xx}(q, \omega)$  in the 1/3 magnetization plateau phase. All results are obtained by DMRG-TDVP calculations for a system with length  $L = 120$ , and the color coding of  $\mathcal{S}^{xx}(q, \omega)$  uses a piecewise function with a boundary value  $U_0 = 2$ . The dispersion lines, distinguished by colors and numerical labels, correspond to various localized excitations within a single trimer. (1)(2)(4) are the excitations from  $|0\rangle \rightarrow |1\rangle$ ,  $|0\rangle \rightarrow |3\rangle$  and  $|0\rangle \rightarrow |6\rangle$  with  $\Delta M = -1$ , respectively. (3) is the excitations from  $|0\rangle \rightarrow |4\rangle$  with  $\Delta M = 1$ .

tization plateau phases. In the XY-I phase with a small  $g$ , a weak magnetic field induces an incommensurate ground state with slight magnetization. By utilizing the ground state  $|0\rangle$  and the first excited state  $|1\rangle$  of a single trimer, we can construct an approximate ground state with antiferromagnetic order, such as  $|\psi\rangle_g = |0101\dots 01\rangle$ . Consequently, we are able to calculate the dispersion relations corresponding to the intermediate-energy and high-energy excitations with  $|\Delta M| = 1$  by employing only  $N = 4$  trimers, details can be found in Supplementary note 6. Regarding the intermediate-energy excitations, four dispersion relations emerge at  $\omega \propto J_1$ , as shown in Fig. 3(e), which describe the localized excitations from  $|0\rangle$  to  $|3\rangle$ ,

$$\epsilon_D(q) = \begin{cases} -\frac{1}{3}g \cos(3q) + \mathbb{E}_1 - \mathbb{E}_0 + H_z - \frac{1}{9}g, \\ -\frac{2}{9}g \cos(3q) + \mathbb{E}_1 - \mathbb{E}_0 + H_z, \\ -\frac{2}{9}g \cos(3q) + \mathbb{E}_1 - \mathbb{E}_0 + H_z + \frac{2}{9}g, \\ -\frac{2}{9}g \cos(3q) + \mathbb{E}_1 - \mathbb{E}_0 + H_z + \frac{2}{9}g. \end{cases} \quad (11)$$

It can be observed that these dispersion relations depend on the energy gap  $\mathbb{E}_1 - \mathbb{E}_0$  between the ground state and first excited-state energies of one single trimer in the absence of magnetic field, and they increase with the application of magnetic field  $H_z$ . In comparison to the case  $H_z = 0$  [11], only one branch of doublons remains under the influence of magnetic field; thus, the intermediate-energy excitation corresponds to the generation of doublons. These dispersion lines do not align well with the spectrum due to the approximation of the ground state. Additionally, we observe a continuum that may origi-

nate from bound spinons. The central doublet, which is dressed by these spinons, propagates through the system, resulting in various internal modes of these composite excitations. This, in turn, leads to a band of finite width in the energy of these excitations. For further details, see the propagation of doublons in Supplementary note 2.

For the high-energy excitations, the application of a magnetic field results in the division of the spectrum into two distinct branches, as shown in Figs. 3(a)(e). Both branches originate from the high-energy internal trimer excitations. We designate the upper branch (excitation from  $|0\rangle$  to  $|6\rangle$ ) as the upper quarton, and the lower one (excitation from  $|0\rangle$  to  $|4\rangle$ ) as the lower quarton. The dispersion relations for the upper quarton are given by,

$$\epsilon_{UQ}(q) = \begin{cases} \frac{1}{18}g \cos(3q) + \mathbb{E}_2 - \mathbb{E}_0 + H_z - \frac{1}{6}g, \\ \frac{2}{9}g \cos(3q) + \mathbb{E}_2 - \mathbb{E}_0 + H_z - \frac{1}{6}g, \\ \frac{2}{9}g \cos(3q) + \mathbb{E}_2 - \mathbb{E}_0 + H_z + \frac{1}{6}g, \end{cases} \quad (12)$$

and the ones for lower quarton are given by,

$$\epsilon_{LQ}(q) = \begin{cases} \frac{1}{6}g \cos(3q) + \mathbb{E}_2 - \mathbb{E}_0 - H_z + \frac{1}{18}g, \\ \frac{2}{9}g \cos(3q) + \mathbb{E}_2 - \mathbb{E}_0 - H_z + \frac{1}{18}g, \\ \frac{2}{9}g \cos(3q) + \mathbb{E}_2 - \mathbb{E}_0 - H_z + \frac{1}{6}g. \end{cases} \quad (13)$$

These dispersion relations depend on the energy gap  $\mathbb{E}_2 - \mathbb{E}_0$  between the ground state and second excited-state energies of one single trimer in the absence of magnetic field, and they exhibit a significant concordance

with the DMRG-TDVP results concerning the positioning of these excitations and their bandwidths. This alignment indicates the conceptualization of localized excitations is valid, despite the fact that the calculation relies on a rather coarse approximation of the ground state. Consequently, the high-energy quartons remain persist in the XY-I phase at low values of  $g$ .

In the  $1/3$  magnetization plateau phase, each trimer exhibits an effective magnetic quantum number  $1/2$ , resembling a polarized spin as a unit cell. We can construct the ground state of the  $1/3$  magnetization plateau using the ground state of single trimer,  $|\psi\rangle_g = |000\dots 00\rangle$ , to study the spin dynamics. The low-energy spin wave is generated by the flipping of one spin within the ferromagnetic state, a phenomenon effectively described by the propagation of magnons. In this scenario, we can manipulate the effective spin of one trimer; for instance, by altering one trimer from  $|0\rangle$  to  $|1\rangle$  in state  $|\psi\rangle_g$ , that results in the dispersion relation,

$$\epsilon^{(1)}(q) = \frac{4}{9}g \cos(3q) + H_z - \frac{4}{9}g, \quad (14)$$

which coincides well with the low-energy excitation spectrum, irrespective of the magnitude of the magnetic field, as illustrated in Fig. 5. We designate this excitation as the reduced spin wave inspired of the conventional magnon picture. Moving on to the intermediate-energy excitations, where one trimer is excited from  $|0\rangle$  to  $|3\rangle$  with  $\Delta M = 1$ , the associated dispersion relation is

$$\epsilon^{(2)}(q) = -\frac{1}{3}g \cos(3q) + \mathbb{E}_1 - \mathbb{E}_0 + H_z - \frac{2}{9}g. \quad (15)$$

Here, the intermediate-energy mode is termed as the doublon rather than the magnon, as it arises from the excitation of localized trimers and exhibits a higher energy gap compared to the low-energy magnon. For the high-energy excitations, two distinct branches of the excitation spectra emerge, which corresponds to the excitation  $|0\rangle \rightarrow |6\rangle$  with  $\Delta M = -1$  and  $|0\rangle \rightarrow |4\rangle$  with  $\Delta M = 1$ . The corresponding dispersion relations are given by,

$$\epsilon^{(3)}(q) = \frac{1}{6}g \cos(3q) + \mathbb{E}_2 - \mathbb{E}_0 - H_z + \frac{1}{9}g, \quad (16)$$

$$\epsilon^{(4)}(q) = \frac{1}{18}g \cos(3q) + \mathbb{E}_2 - \mathbb{E}_0 + H_z - \frac{1}{3}g, \quad (17)$$

which are referred to as the high-energy quartons. Notably, it can be observed that the reduced spin wave ( $|0\rangle \rightarrow |1\rangle$ ), doublon ( $|0\rangle \rightarrow |3\rangle$ ) and upper quarton ( $|0\rangle \rightarrow |6\rangle$ ) share the same magnetization quantum number  $\Delta M = -1$ , and they collectively increase in energy as the magnetic field intensifies. Conversely, the lower quarton descends independently due to its distinct magnetization quantum number  $\Delta M = 1$ , ultimately becoming the low-energy spectrum when  $H_z \geq 0.9$ . More interestingly, as shown in Figs. 3(c)(g), it is noteworthy that even in the XY-II phase, the excitations characterized by  $\Delta M = -1$  remain observable in the high-energy regime.

## E. Quantum magnets

It has been discovered that  $\text{Na}_2\text{Cu}_3\text{Ge}_4\text{O}_{12}$  is an ideal realization of the spin- $1/2$  antiferromagnetic trimer chain, wherein  $\text{Cu}_3\text{O}_8$  comprises the trimers formed by three edge-sharing  $\text{CuO}_4$  square planes arranged linearly. The magnetic  $\text{Cu}^{2+}$  ions within the  $\text{CuO}_4$  square planes demonstrate quantum spin- $1/2$  characteristics [12, 59]. Fig. 6(a) presents a more realistic spin model that incorporates an additional next-nearest neighbor intratrimer exchange coupling  $J_3$ . The Hamiltonian for this system is given by

$$\mathcal{H}' = \sum_{i=1}^N [J_1 (\mathbf{S}_{i,a} \cdot \mathbf{S}_{i,b} + \mathbf{S}_{i,b} \cdot \mathbf{S}_{i,c}) + J_2 \mathbf{S}_{i,c} \cdot \mathbf{S}_{i+1,a} + J_3 \mathbf{S}_{i,a} \cdot \mathbf{S}_{i,c}] - H_z \sum_{j=1}^{3N} S_j^z, \quad (18)$$

where the experimental measurements have established the coupling strengths as  $J_1 = 235K$  and  $J_2 = J_3 = 0.18J_1$ . When  $H_z = 0$ , the eight energy levels (see Fig. 6(c)) reduce to three ones,  $E'_0 = -0.955J_1$ ,  $E'_1 = -0.135J_1$  and  $E'_2 = 0.545J_1$ . The doublon and quarton manifest at  $\omega \sim E'_1 - E'_0 = 0.82J_1$  and  $\omega \sim E'_2 - E'_0 = 1.5J_1$ , respectively, as shown in Fig. 6(e). In the inelastic neutron scattering measurements conducted on  $\text{Na}_2\text{Cu}_3\text{Ge}_4\text{O}_{12}$  [12], three excitation modes have been identified. The two-spinon modes are observed below 5 meV, while, the doublon and quarton states appear in the intermediate (17 – 22 meV) and high (32 – 37 meV) energy ranges, respectively. These findings are corroborated by the intermediate-energy (at  $\omega \sim 0.82J_1$ ) and high-energy (at  $\omega \sim 1.5J_1$ ) excitations observed in our numerical simulations.

In Fig. 6(b), the application of a magnetic field results in the splitting of the three energy levels of a single trimer into eight distinct levels. When  $H_z \leq 1.5$ , the ground state is  $|0\rangle$  with an energy of  $E_0 = -0.955J_1 - H_z/2$ . Although the antiferromagnetic interaction  $J_3$  competes with the interaction  $J_1$  and induces frustration within the spin system, when  $J_3 \leq J_1$ , introducing  $J_3$  does not change the relative sequence of energy levels and their quantum numbers. There are only minor shifts in their eigenvalues, as depicted in Fig. 6(c). Thus, the spin excitations can still be characterized by the quasiparticles doublons and quartons. The trimer chain subjected to the  $J_3$  interaction continues to display a  $1/3$  magnetization plateau, as shown in Fig. 6(d). Experimental measurements have confirmed the presence of  $1/3$  magnetization plateau above 28 Tesla [12], which aligns with our DMRG calculations. Although the phase diagram and  $1/3$  magnetization plateau have been elucidated [12], significantly less is understood regarding the evolution of intermediate-energy and high-energy excitations under the influence of a magnetic field. In this subsection, we present the excitation spectrum of the model depicted in Fig. 6(a), which is pertinent to the material



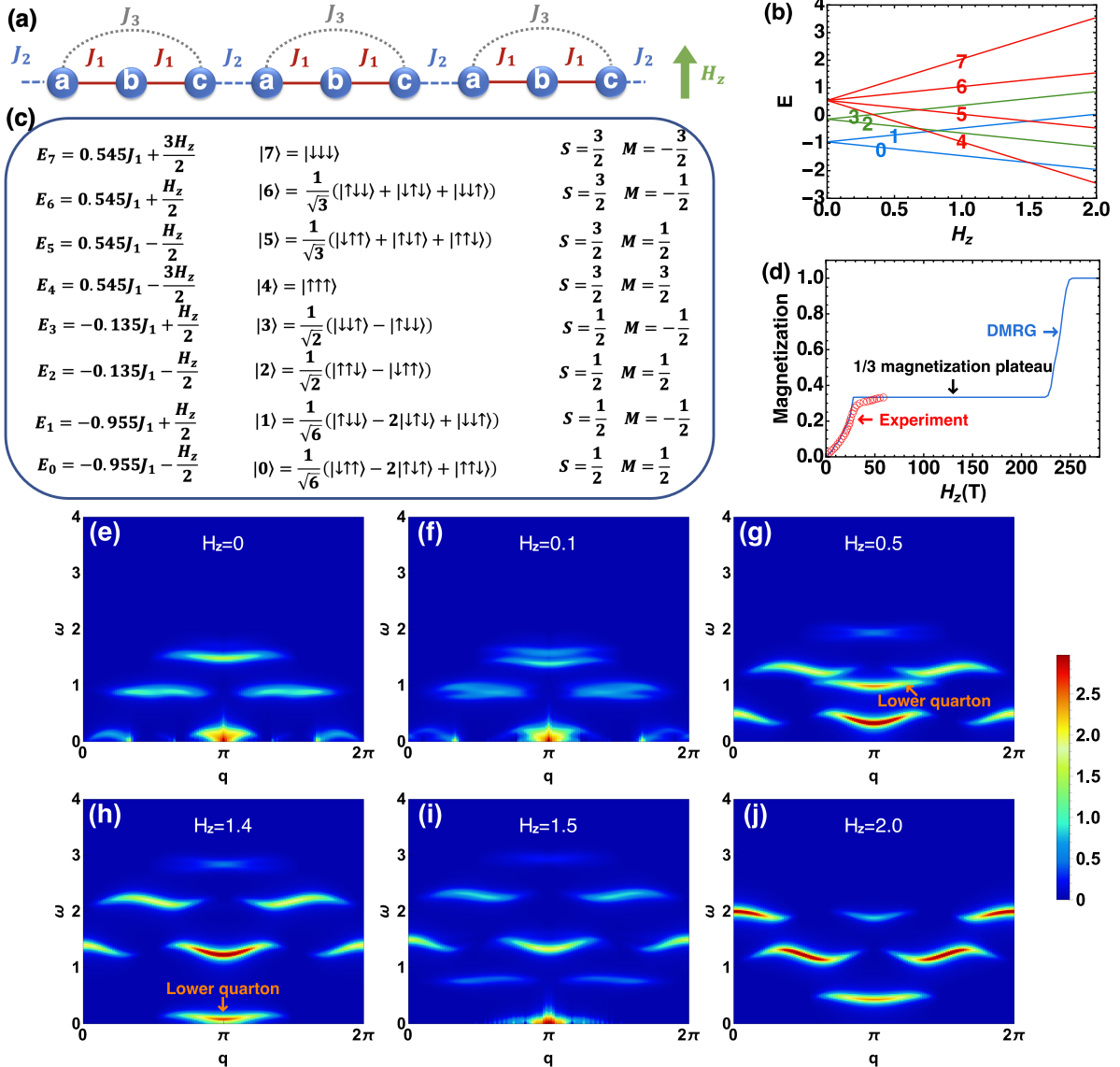


FIG. 6. **Trimer model related to the experimental material  $\text{Na}_2\text{Cu}_3\text{Ge}_4\text{O}_{12}$ .** (a) Schematic representation of the trimer model with next-nearest neighbor intratrimer exchange couplings  $J_3$ , and  $J_2 = J_3 = 0.18J_1$ . The spins labeled as  $a, b$  and  $c$  are the three  $\text{Cu}^{2+}$  spins within a trimer unit. (b) Energy levels as functions of the magnetic field  $H_z$ . (c) Eigenenergies, wave functions, and quantum numbers of an isolated trimer unit in the material under the magnetic field  $H_z$ . (d) The magnetization curves obtained by experimental measurements and DMRG calculation, with the results normalized to the maximum of magnetization. The experimental data is extracted from Fig.1d in Ref.[12].  $\mathcal{S}^{xx}(q, \omega)$  of spin model related to experimental materials  $\text{Na}_2\text{Cu}_3\text{Ge}_4\text{O}_{12}$  in (e) the case without magnetic field, (f) XY-I phase, (g)(h) 1/3 magnetization plateau phase, (i) XY-II phase, and (j) Ferromagnetic phase obtained by DMRG-TDVP calculation for  $L = 120$ . The color coding of  $\mathcal{S}^{xx}(q, \omega)$  uses a piecewise function with a boundary value  $U_0 = 2$ .

$\text{Na}_2\text{Cu}_3\text{Ge}_4\text{O}_{12}$ . Due to the weak  $J_3$ , the spin excitations in four phases displayed in Figs. 6(f)-(j) exhibit similarities to those of a trimer chain devoid of  $J_3$ . This includes the separation of high-energy spectra, the presence of gapless excitations in the XY-I and XY-II phases, and the emergence of a gap at the edges of Brillouin zones in the Ferromagnetic phase. Our theoretical results concerning the high-energy quasiparticles excitations under the magnetic field can be directly validated through the

inelastic neutron scattering experiments on the material  $\text{Na}_2\text{Cu}_3\text{Ge}_4\text{O}_{12}$ .

The realization of doublon and quarton in specific experimental materials drives us to think deeper into how we might manipulate these excitations and explore their possible applications. Among that, the BEC of doublon or quarton is quite an important topic. BEC represents a compelling state of matter that has been observed in bosonic atoms and cold gases. Quasiparticles associated

with magnetic excitations, which possess integer spin and adhere to Bose statistics, such as the magnon and triplon, are integral to the study of BEC [60–63]. In particular, in the dimerized antiferromagnets like  $\text{TlCuCl}_3$ , the intradimer interaction is stronger than the interdimer interaction, thereby an isolated dimer exhibits a singlet ground state characterized by a total spin  $S = 0$  and a triplet excited state with spin  $S = 1$ . Due to the relatively weak interdimer interaction, the magnetic excitations are predominantly governed by triplons. After applying a magnetic field, the Zeeman term controls the density of triplons, resulting in a decrease in energy for the triplon with a magnetic quantum number  $S^z = 1$ . At a critical magnetic field  $H_{C1}$ , the energy of the triplons reaches zero, leading to their gradual condensation into the ground state until a second critical magnetic field  $H_{C2}$  is attained. Beyond  $H_{C2}$ , all spins become polarized.

Inspired by the triplon BEC phenomenon, it is pertinent to inquire that whether quarton BEC can be observed in trimerized systems. In this context, we present a preliminary analysis of quarton BEC based on our findings. Firstly, the high-energy quartons arise from the internal trimer excitations and possess an integer spin quantum number  $S = 1$ , thereby conforming the Bose statistics. Secondly, the application of a magnetic field causes the lower branch of quartons to approach zero energy, as show in Fig. 5 and Figs. 6(g)(h). At the critical point  $H_{C1}$ , which delineates the transition between the 1/3 magnetization plateau phase and the XY-II phase, the lower quartons commence condensation and accumulation as the magnetic field intensifies within the XY-II phase.

Furthermore, although the BEC is more possible to be observed in the real materials exhibiting 3D spin systems, the 1D and 2D limits can serve as effective starting points for comprehending the field-induced quasiparticle BEC [62–65]. In the context of 1D systems, it is well-established that BEC does not occur due to the significant quantum fluctuations. For 2D systems, the presence of a finite density of states at zero energy poses a barrier to form the BEC. Nevertheless, the critical exponents associated with the 1D or 2D quantum critical points can be observed over a substantial temperature range [62]. In the 2D quantum dimer magnets, both the critical field and the critical temperature of the BEC dome can be accurately characterized [65]. Consequently, the studies of 1D and 2D systems are instrumental in the exploration of quasiparticle BEC. Our recent investigation into spin dynamics in 2D trimer systems has revealed the emergence of high-energy quartons [22]. These 2D trimer systems offer valuable platforms for further examination of the quarton BEC. Moreover, a small but finite interlayer coupling in a quasi-2D magnet stabilizes marginal BEC [63]. Therefore, a field-induced quarton BEC may emerge in the quantum material  $\text{Na}_2\text{Cu}_3\text{Ge}_4\text{O}_{12}$ . However, a technical challenge arises due to the fact that the critical magnetic field  $H_{C1}$  (see Fig. 6(d)) may exceed the

limits of experimental accessibility. Therefore, only the transition between the XY-I phase and the 1/3 magnetization plateau phase can be realized in  $\text{Na}_2\text{Cu}_3\text{Ge}_4\text{O}_{12}$  through the currently available magnetic field. A quantum material characterized by trimer structures and relatively weak intratrimer interactions is essential to experimentally investigate the quarton BEC. Theoretically, it is of interest to seek further evidence of quarton BEC by examining the  $(T, H_z)$  phase diagram and the power-law temperature dependence of thermodynamic properties in both 2D and 3D trimer systems in future studies.

### III. DISCUSSION

In summary, we have utilized the ED, CPT and DMRG-TDVP methods to investigate the quantum phase transition and spin dynamics of the antiferromagnetic trimer chain subjected to a longitudinal magnetic field. Our findings reveal that the interplay of magnetic field and interaction leads to the emergence of four distinct phases: XY-I, 1/3 magnetization plateau, XY-II, and ferromagnetic phases. By mapping the entanglement entropy onto the parameter space  $(g, H_z)$ , we obtain a comprehensive phase diagram. Furthermore, it has been confirmed that the critical phases XY-I and XY-II phases are both characterized by the conformal field theory with a central charge  $c \simeq 1$ . The transitions between these phases are identified as the second-order quantum phase transitions.

In the context of transverse and longitudinal excitations of a trimer chain subjected to a magnetic field, we have determined that the incommensurate wave numbers corresponding to zero energy are dependent of the magnetization in the XY-I and XY-II phases. In addition, we have observed the presence of gapped excitations within both the 1/3 magnetization plateau and ferromagnetic phases. Specifically, a continuum of excitations is observed in the high-energy regime of the 1/3 magnetization plateau phase. In the ferromagnetic phases, the excitations continue to be characterized by spin waves, however, magnons located at the edges of the Brillouin zone exhibit two diverse energies for the same wave vector.

Furthermore, we have identified the intermediate-energy and high-energy excitations for small  $g$ , and have elucidated their excitation mechanisms within the XY-I and 1/3 magnetization plateau phases by analyzing their dispersion relations. In these phases, the intermediate-energy and high-energy modes correspond to the propagating internal trimer excitations, referred to as doublons and quartons, respectively. In comparison to the trimer chain in the absence of a magnetic field, the high-energy spectrum exhibits a splitting two branches, which correspond to the upper quarton and lower quarton, respectively. As the magnetic field increases, the gap between these two branches widens, resulting in the lower quarton becoming the low-energy spectrum.

Experimentally, there are existing examples of

coupled-trimer quantum magnets, such as  $A_3Cu_3(PO_4)_4$  ( $A = \text{Ca, Sr, Pb}$ ) [27–30] and  $Na_2Cu_3Ge_4O_{12}$  [12]. Although the trimers in  $Pb_3Cu_3(PO_4)_4$  do not exhibit a linear arrangement, two flat excitations at approximately  $\omega \sim 9meV$  and  $\omega \sim 13.5meV$  have been observed in the inelastic neutron-scattering spectra measured at 8K [27]. These excitations are closely associated with the intermediate-energy (at  $\omega \sim J_1$ ) and the high-energy (at  $\omega \sim 1.5J_1$ ) excitations in the trimer chain without magnetic field [11]. Additionally, for the quantum magnet  $Na_2Cu_3Ge_4O_{12}$ , an additional next-nearest neighbor interaction is present within the trimers; however, its strength is relatively weak, and the wave functions and quantum numbers of a single trimer remain invariant. Consequently, the doublons and quartons have been observed in the inelastic neutron-scattering experiments [12]. We have theoretically demonstrated that doublons and quartons remain observable in the trimer chain under a magnetic field, even with the introduction of the interaction  $J_3$ . These findings can be directly investigated through the inelastic neutron-scattering experiments conducted on the aforementioned quantum materials. Moreover, based on the results obtained from the 1D trimer chain under a magnetic field, it is probable that the quarton BEC may be identified in experiments once suitable materials are found. Our results will be instrumental in interpreting inelastic neutron scattering and other experiments that probe the high-energy excitations beyond spin waves and spinons, as well as in facilitating detailed investigations of coexisting exotic excitations.

## IV. METHODS

### A. Matrix product states

DSF is a significant physical quantity for studying spin dynamics, a process that has been effectively facilitated by the DMRG in conjunction with the time evolution algorithms [37, 66–70]. In this article, we primarily employ the TDVP method to handle with the time evolution of many-body systems [39, 40]. Specifically, we conduct DMRG-TDVP calculations on a finite chain with open boundary conditions to analyze the spectrum. We denote the ground state of the trimer chain in the presence of a magnetic field as  $|\mathcal{G}\rangle$ , which allows us to compute the real time evolution of the correlation function,

$$\langle \mathcal{G} | S_j^\alpha(t) S_0^\beta(0) | \mathcal{G} \rangle = e^{iE_0 t} \langle \mathcal{G} | S_j^\alpha e^{-i\mathcal{H}t} S_0^\beta | \mathcal{G} \rangle, \quad (19)$$

for various times  $t$  and distances  $j$ .  $E_0$  represents the ground state energy. We select the site at the center of the chain designated as the site index 0. Firstly, we obtain the ground state  $|\mathcal{G}\rangle$  by employing the DMRG method. Subsequently, we introduce a local perturbation  $\hat{S}_0^\beta$  at the center of the spin chain to generate the initial state

$$|\phi\rangle = \hat{S}_0^\beta |\mathcal{G}\rangle \quad (20)$$

for real-time evolution. The real-time evolution state

$$|\phi(t)\rangle = e^{-i\mathcal{H}t} |\phi\rangle \quad (21)$$

is carried out using the single-site TDVP with a time step of  $dt = 0.05J_1^{-1}$  and a maximum time  $t_{\max} = 200J_1^{-1}$ . Finally, a Fourier transformation is performed to obtain  $S^{\alpha\beta}(q, \omega)$

$$S^{\alpha\beta}(q, \omega) = \sum_j e^{-iqj} \left[ \int_{-\infty}^{\infty} dt e^{i\omega t} \langle \hat{S}_j^\alpha(t) \hat{S}_0^\beta \rangle \right]. \quad (22)$$

Technically, to mitigate the limitations imposed by the finite-time limit constraint on the resolution of the spectral functions in frequency space, a Gaussian windowing function, expressed as  $\exp[-4(t/t_{\max})^2]$ , is incorporated in the reconstruction of the DSF [37]. During the DMRG calculations, we set  $\varepsilon_{\text{SVD}} = 10^{-11}$  and retained a maximum of 6000 states. The time evolution is executed on a chain with open boundary conditions and  $N = 120$  spins, which is sufficiently large to mitigate finite-size effects, with the maximum bond dimension set to 2000. All MPS simulations are performed using the ITensor library [71].

### B. Cluster perturbation theory

Cluster perturbation theory (CPT) is a theoretical framework used to study the electronic and magnetic properties of strongly correlated electrons [41–44], especially for calculating the single-particle spectral functions of Hubbard-type fermionic models and the dynamical spin structure factors of Heisenberg models. The fundamental concept of CPT involves partitioning a large system into smaller clusters, accurately calculating the properties of these clusters, and then use the mean-field and perturbation theory to infer the properties of the entire system. Here, we employ ED as a computational method to determine the dynamical spin structure factor within the cluster framework. Following Ref. 44, we provide a concise overview of the procedural steps involved in applying cluster perturbation theory to spin models.

Firstly, we transform the spin model into a hard-core boson model through the application of the following mapping,

$$S_i^+ = b^\dagger, S_i^- = b, S_i^z = b_i^\dagger b_i - 1/2, \quad (23)$$

Then the Hamiltonian can be rewritten as,

$$\begin{aligned}
\mathcal{H} = & \sum_{i=1}^N \left( \frac{J_1}{2} b_{i,a}^\dagger b_{i,b} + \frac{J_1}{2} b_{i,b}^\dagger b_{i,c} + \frac{J_2}{2} b_{i,c}^\dagger b_{i+1,a} + H.c. \right) \\
& + \sum_{i=1}^N [J_1 n_{i,a} n_{i,b} + J_1 n_{i,b} n_{i,c} + J_2 n_{i,c} n_{i+1,a}] \\
& - \left( H_z + \frac{J_1 + J_2}{2} \right) \sum_{i=1, i \in a/c}^N n_i \\
& - (H_z + J_1) \sum_{i=1, i \in b}^N n_i + \mathcal{H}_{\text{const.}}, \tag{24}
\end{aligned}$$

where the  $b_i^\dagger$ ,  $b_i$  and  $n_i = b_i^\dagger b_i$  are the bosonic operators with hard-core constraint  $n_i = 0$  or 1.

Secondly, we split the system into clusters. In our calculations, the cluster size is chosen to be  $N = 8$ ,  $L = 24$  which is sufficiently large to yield the accurate results. For the interaction bonds connecting adjacent clusters. We use self-consistent mean-field treatment to decouple the interactions between the clusters,

$$J_2 n_{1,c} n_{N,a} \approx J_2 (\langle n_{1,a} \rangle n_{N,c} + \langle n_{N,c} \rangle n_{1,a}). \tag{25}$$

Thirdly, we employ exact diagonalization to self-consistently obtain the mean-field potentials of the two end sites,  $\langle n_{1,c} \rangle$  and  $\langle n_{N,c} \rangle$ . And after the convergence, we run a ED simulation to obtain the real-frequency single-particle Green function matrix  $\mathbf{G}_{ij}^C(\omega)$  using the Lanczos iteration method, where  $C$  denotes the Green function matrix of the cluster.

Fourthly, the original lattice Green function matrix can be derived from the cluster Green function matrix by disregarding the nonlocal self-energy contributions between clusters.

$$\mathbf{G}^{L,-1}(\tilde{q}, \omega) = \mathbf{G}^{C,-1}(\omega) - V(\tilde{q}). \tag{26}$$

where  $L$  denotes the Green function matrix of the original lattice,  $\tilde{\mathbf{q}}$  is the wave vector within the Brillouin zone of the supercell formed by the cluster.

Fifthly, we perform the reperiodization of the Green function matrix to restore translational invariance.

$$G_{\text{CPT}}(q, \omega) = \frac{1}{N_s} \sum_{ij} e^{-i\mathbf{q}(\mathbf{r}_i - \mathbf{r}_j)} G_{ij}^L(\omega). \tag{27}$$

Then the transverse dynamical spin structure factor can be obtained via

$$S^{+-}(q, \omega) = -\frac{1}{\pi} \text{Im} G_{\text{CPT}}(q, \omega). \tag{28}$$

The cluster perturbation theory applied to spin models has been successfully applied to investigate the  $J_1 - J_2$  and  $J_1 - J_3$  models on a 2D square lattice [44, 72], the  $J_1 - J_2$  model on honeycomb lattice [73], as well as 2D trimer models [22]. This methodology demonstrates efficacy in characterizing the continua present in quantum

spin liquid phases, as well as the magnon and triplon excitations observed in conventional Néel and valence bond solid phases. The method is exact in two limiting scenarios: one in which the interactions between clusters approach zero or are exceedingly weak, and the other in which cluster size approaches infinity or is significantly large. In the context of our trimer chain model, when  $g = J_2/J_1$  is small, accurate results can be achieved even with relatively small clusters, such as  $N = 2, 4$ . The selection of a cluster size of  $N = 8$  in our study ensures accuracy across both small and large  $g$  regimes. This cluster size is sufficiently large to guarantee precision across a wide range of parameter values.

## V. DATA AVAILABILITY

The data that support the findings of this study are available from the corresponding authors upon reasonable request.

## VI. CODE AVAILABILITY

The code used for the analysis is available from the authors upon reasonable request.

## ACKNOWLEDGMENTS

We like to thank Zijian Xiong for fruitful discussions. This project is supported by the National Key R&D Program of China, Grants No. 2022YFA1402802, No. 2018YFA0306001, NSFC-92165204, NSFC-11974432, and Shenzhen Institute for Quantum Science and Engineering (Grant No. SIQSE202102), Guangdong Provincial Key Laboratory of Magnetoelectric Physics and Devices (No. 2022B1212010008), and Guangdong Fundamental Research Center for Magnetoelectric Physics. J.Q.C. is supported by the National Natural Science Foundation of China through Grants No. 12047562. H.Q.W. is supported by the National Natural Science Foundation of China through Grants No. 12474248, Guangdong Basic and Applied Basic Research Foundation (No. 2023B1515120013) and Youth S&T Talent Support Programme of Guangdong Provincial Association for Science and Technology (GDSTA) (No. SKXRC202404). J.Q.C. also acknowledges the financial support from the Special Project in Key Areas for Universities in Guangdong Province (No. 2023ZDZX3054) and the Dongguan Key Laboratory of Artificial Intelligence Design for Advanced Materials (DKL-AIDAM).

## VII. AUTHOR CONTRIBUTIONS

D.X.Y., H.Q.W., and J.Q.C. conceived and designed the project. J.Q.C., H.Q.W. and Z.Y.N. performed the

numerical simulations. D.X.Y., J.Q.C., H.Q.W., and Z.Y.N. provided the explanation of the numerical results. All authors contributed to the discussion of the results and wrote the paper.

### VIII. COMPETING INTERESTS

The authors declare no competing interests.

### IX. REFERENCES

- 
- [1] Mikeska, H.-J. & Kolezhuk, A. K. *One-dimensional magnetism*, 1–83 (Springer Berlin Heidelberg, Berlin, Heidelberg, 2004).
- [2] Karbach, M., Müller, G., Bougourzi, A. H., Fledderjohann, A. & Mütter, K.-H. Two-spinon dynamic structure factor of the one-dimensional  $S = 1/2$  Heisenberg antiferromagnet. *Phys. Rev. B* **55**, 12510–12517 (1997).
- [3] Tennant, D. A., Perring, T. G., Cowley, R. A. & Nagler, S. E. Unbound spinons in the  $S = 1/2$  antiferromagnetic chain  $\text{KCuF}_3$ . *Phys. Rev. Lett* **70**, 4003 (1993).
- [4] Lake, B. *et al.* Multispinon continua at zero and finite temperature in a near-ideal Heisenberg chain. *Phys. Rev. Lett.* **111**, 137205 (2013).
- [5] Enderle, M. *et al.* Two-spinon and four-spinon continuum in a frustrated ferromagnetic spin-1/2 chain. *Phys. Rev. Lett.* **104**, 237207 (2010).
- [6] Klauser, A., Mossel, J., Caux, J.-S. & van den Brink, J. Spin-exchange dynamical structure factor of the  $S = 1/2$  Heisenberg chain. *Phys. Rev. Lett.* **106**, 157205 (2011).
- [7] Schlappa, J. *et al.* Probing multi-spinon excitations outside of the two-spinon continuum in the antiferromagnetic spin chain cuprate  $\text{Sr}_2\text{CuO}_3$ . *Nat. Commun.* **9**, 5394 (2018).
- [8] Kohno, M. Dynamically dominant excitations of string solutions in the spin-1/2 antiferromagnetic Heisenberg chain in a magnetic field. *Phys. Rev. Lett.* **102**, 037203 (2009).
- [9] Wang, Z. *et al.* Experimental observation of Bethe strings. *Nature* **554**, 219–223 (2018).
- [10] Wang, Z. *et al.* Quantum critical dynamics of a Heisenberg-Ising chain in a longitudinal field: Many-body strings versus fractional excitations. *Phys. Rev. Lett.* **123**, 067202 (2019).
- [11] Cheng, J.-Q. *et al.* Fractional and composite excitations of antiferromagnetic quantum spin trimer chains. *npj Quantum Mater.* **7**, 1–11 (2022).
- [12] Bera, A. K. *et al.* Emergent many-body composite excitations of interacting spin-1/2 trimers. *Nat. Commun.* **13**, 6888 (2022).
- [13] Do, S.-H. *et al.* Understanding temperature-dependent  $\text{SU}(3)$  spin dynamics in the  $S = 1$  antiferromagnet  $\text{Ba}_2\text{FeSi}_2\text{O}_7$ . *npj Quantum Mater.* **8**, 5 (2023).
- [14] Han, J.-H. *et al.* Weak-coupling to strong-coupling quantum criticality crossover in a kitaev quantum spin liquid  $\alpha - \text{RuCl}_3$ . *npj Quantum Mater.* **8**, 33 (2023).
- [15] Headings, N. S., Hayden, S. M., Coldea, R. & Perring, T. G. Anomalous high-energy spin excitations in the High- $T_c$  superconductor-parent antiferromagnet  $\text{La}_2\text{CuO}_4$ . *Phys. Rev. Lett.* **105**, 247001 (2010).
- [16] Zhou, K.-J. *et al.* Persistent high-energy spin excitations in iron-pnictide superconductors. *Nat. Commun.* **4**, 1470 (2013).
- [17] Ishii, K. *et al.* High-energy spin and charge excitations in electron-doped copper oxide superconductors. *Nat. Commun.* **5**, 3714 (2014).
- [18] Song, Y. *et al.* High-energy magnetic excitations from heavy quasiparticles in  $\text{CeCu}_2\text{Si}_2$ . *npj Quantum Mater.* **6**, 60 (2021).
- [19] Shao, H. *et al.* Nearly deconfined spinon excitations in the square-lattice spin-1/2 Heisenberg antiferromagnet. *Phys. Rev. X* **7**, 041072 (2017).
- [20] Dalla Piazza, B. *et al.* Fractional excitations in the square-lattice quantum antiferromagnet. *Nat. Phys.* **11**, 62–68 (2015).
- [21] Gu, C., Gu, Z.-L., Yu, S.-L. & Li, J.-X. Spectral evolution of the  $s = \frac{1}{2}$  antiferromagnetic Heisenberg model: From one to two dimensions. *Phys. Rev. B* **108**, 224418 (2023).
- [22] Chang, Y.-Y., Cheng, J.-Q., Shao, H., Yao, D.-X. & Wu, H.-Q. Magnon, doublon and quarton excitations in 2D trimerized Heisenberg models. *Front. Phys.* **19**, 63202 (2024).
- [23] Dagotto, E. & Rice, T. M. Surprises on the way from one- to two-dimensional quantum magnets: The ladder materials. *Science* **271**, 618 (1996).
- [24] Haldane, F. D. M. Continuum dynamics of the 1-D Heisenberg antiferromagnet: Identification with the  $\phi(3)$  nonlinear sigma model. *Phys. Lett. A* **93**, 464–468 (1983).
- [25] Schmidiger, D. *et al.* Symmetric and asymmetric excitations of a strong-leg quantum spin ladder. *Phys. Rev. B* **88**, 094411 (2013).
- [26] Doretto, R. L. & Vojta, M. Quantum magnets with weakly confined spinons: Multiple length scales and quantum impurities. *Phys. Rev. B* **80**, 024411 (2009).
- [27] Matsuda, M. *et al.* Magnetic excitations from the linear Heisenberg antiferromagnetic spin trimer system  $\text{A}_3\text{Cu}_3(\text{PO}_4)_4$  ( $\text{A} = \text{Ca}, \text{Sr}$ , and  $\text{Pb}$ ). *Phys. Rev. B* **71**, 144411 (2005).
- [28] Drillon, M. *et al.* 1D ferrimagnetism in copper (ii) trimetric chains: specific heat and magnetic behavior of  $\text{A}_3\text{Cu}_3(\text{PO}_4)_4$  with  $\text{A} = \text{Ca}, \text{Sr}$ . *J. Magn. Magn. Mater.* **128**, 83–92 (1993).
- [29] Belik, A. A., Matsuo, A., Azuma, M., Kindo, K. & Takano, M. Long-range magnetic ordering of  $s = 1/2$  linear trimers in  $\text{A}_3\text{Cu}_3(\text{PO}_4)_4$  ( $\text{A} = \text{Ca}, \text{Sr}, \text{Pb}$ ). *J. Solid State Chem.* **178**, 709–714 (2005).
- [30] Yamamoto, S. & Ohara, J. Low-energy structure of the homometallic intertwining double-chain ferrimagnets  $\text{A}_3\text{Cu}_3(\text{PO}_4)_4$  ( $\text{A} = \text{Ca}, \text{Sr}, \text{Pb}$ ). *Phys. Rev. B* **76**, 014409

- (2007).
- [31] Montenegro-Filho, R. R., Matias, F. S. & Coutinho-Filho, M. D. Topology of many-body edge and extended quantum states in an open spin chain:  $1/3$  plateau, Kosterlitz-Thouless transition, and Luttinger liquid. *Phys. Rev. B* **102**, 035137 (2020).
- [32] Montenegro-Filho, R. R., Silva-Júnior, E. J. P. & Coutinho-Filho, M. D. Ground-state phase diagram and thermodynamics of coupled trimer chains. *Phys. Rev. B* **105**, 134423 (2022).
- [33] Hasegawa, Y. & Matsumoto, M. Magnetic excitation in interacting spin trimer systems investigated by extended spin-wave theory. *J. Phys. Soc. Jpn.* **81**, 094712 (2012).
- [34] Cao, G. *et al.* Quantum liquid from strange frustration in the trimer magnet  $\text{Ba}_4\text{Ir}_3\text{O}_{10}$ . *npj Quantum Mater.* **5**, 26 (2020).
- [35] Shen, Y. *et al.* Emergence of spinons in layered trimer Iridate  $\text{Ba}_4\text{Ir}_3\text{O}_{10}$ . *Phys. Rev. Lett.* **129**, 207201 (2022).
- [36] White, S. R. Density matrix formulation for quantum renormalization groups. *Phys. Rev. Lett.* **69**, 2863–2866 (1992).
- [37] White, S. R. & Feiguin, A. E. Real-time evolution using the density matrix renormalization group. *Phys. Rev. Lett.* **93**, 076401 (2004).
- [38] Schollwöck, U. The density-matrix renormalization group in the age of matrix product states. *Ann. Phys.* **326**, 96–192 (2011).
- [39] Haegeman, J. *et al.* Time-dependent variational principle for quantum lattices. *Phys. Rev. Lett.* **107**, 070601 (2011).
- [40] Haegeman, J., Lubich, C., Oseledets, I., Vandereycken, B. & Verstraete, F. Unifying time evolution and optimization with matrix product states. *Phys. Rev. B* **94**, 165116 (2016).
- [41] Gros, C. & Valentí, R. Cluster expansion for the self-energy: A simple many-body method for interpreting the photoemission spectra of correlated fermi systems. *Phys. Rev. B* **48**, 418–425 (1993).
- [42] Sénéchal, D., Perez, D. & Pioro-Ladrière, M. Spectral weight of the hubbard model through cluster perturbation theory. *Phys. Rev. Lett.* **84**, 522–525 (2000).
- [43] Maier, T., Jarrell, M., Pruschke, T. & Hettler, M. H. Quantum cluster theories. *Rev. Mod. Phys.* **77**, 1027–1080 (2005).
- [44] Yu, S.-L., Wang, W., Dong, Z.-Y., Yao, Z.-J. & Li, J.-X. Deconfinement of spinons in frustrated spin systems: Spectral perspective. *Phys. Rev. B* **98**, 134410 (2018).
- [45] Amico, L., Fazio, R., Osterloh, A. & Vedral, V. Entanglement in many-body systems. *Rev. Mod. Phys.* **80**, 517–576 (2008).
- [46] Laflorencie, N. Quantum entanglement in condensed matter systems. *Phys. Rep.* **646**, 1–59 (2016). Quantum entanglement in condensed matter systems.
- [47] Cheng, J.-Q., Wu, W. & Xu, J.-B. Multipartite entanglement in an XXZ spin chain with Dzyaloshinskii–Moriya interaction and quantum phase transition. *Quantum Inf. Process.* **16**, 1–20 (2017).
- [48] Goldstein, M. & Sela, E. Symmetry-resolved entanglement in many-body systems. *Phys. Rev. Lett.* **120**, 200602 (2018).
- [49] Cheng, J.-Q. & Xu, J.-B. Multipartite entanglement, quantum coherence, and quantum criticality in triangular and Sierpiński fractal lattices. *Phys. Rev. E* **97**, 062134 (2018).
- [50] Kunkel, P. *et al.* Detecting entanglement structure in continuous many-body quantum systems. *Phys. Rev. Lett.* **128**, 020402 (2022).
- [51] Oshikawa, M., Yamanaka, M. & Affleck, I. Magnetization plateaus in spin chains: “Haldane gap” for half-integer spins. *Phys. Rev. Lett.* **78**, 1984–1987 (1997).
- [52] Sakai, T. & Okamoto, K. Quantum magnetization plateaus of an anisotropic ferrimagnetic spin chain. *Phys. Rev. B* **65**, 214403 (2002).
- [53] Calabrese, P., Campostrini, M., Essler, F. & Nienhuis, B. Parity effects in the scaling of block entanglement in gapless spin chains. *Phys. Rev. Lett.* **104**, 095701 (2010).
- [54] D’Emidio, J., Block, M. S. & Kaul, R. K. Rényi entanglement entropy of critical  $\text{SU}(N)$  spin chains. *Phys. Rev. B* **92**, 054411 (2015).
- [55] Feng, S., Alvarez, G. & Trivedi, N. Gapless to gapless phase transitions in quantum spin chains. *Phys. Rev. B* **105**, 014435 (2022).
- [56] Hallberg, K., Wang, X. Q. G., Horsch, P. & Moreo, A. Critical behavior of the  $S = 3/2$  antiferromagnetic heisenberg chain. *Phys. Rev. Lett.* **76**, 4955–4958 (1996).
- [57] Takayoshi, S. *et al.* Phase transitions and spin dynamics of the quasi-one dimensional Ising-like antiferromagnet  $\text{BaCo}_2\text{V}_2\text{O}_8$  in a longitudinal magnetic field (2023). 2302.03833.
- [58] Wang, Z. *et al.* From confined spinons to emergent fermions: Observation of elementary magnetic excitations in a transverse-field ising chain. *Phys. Rev. B* **94**, 125130 (2016).
- [59] Yasui, Y., Kawamura, Y., Kobayashi, Y. & Sato, M. Magnetic and dielectric properties of one-dimensional array of  $S = 1/2$  linear trimer system  $\text{Na}_2\text{Cu}_3\text{Ge}_4\text{O}_{12}$ . *J. Appl. Phys.* **115**, 17E125 (2014).
- [60] Rüegg, C. *et al.* Bose–Einstein condensation of the triplet states in the magnetic insulator  $\text{TlCuCl}_3$ . *Nature* **423**, 62–65 (2003).
- [61] Giamarchi, T., Rüegg, C. & Tchernyshyov, O. Bose–Einstein condensation in magnetic insulators. *Nat. Phys.* **4**, 198–204 (2008).
- [62] Zapf, V., Jaime, M. & Batista, C. Bose-Einstein condensation in quantum magnets. *Rev. Mod. Phys.* **86**, 563 (2014).
- [63] Matsumoto, Y. *et al.* A quantum critical bose gas of magnons in the quasi-two-dimensional antiferromagnet  $\text{YbCl}_3$  under magnetic fields. *Nat. Phys.* **20**, 1131–1138 (2024).
- [64] Volkov, P. A., Gazit, S. & Pixley, J. H. Magnon Bose–Einstein condensation and superconductivity in a frustrated kondo lattice. *Proc. Nat. Acad. Sci.* **117**, 20462–20467 (2020).
- [65] Feng, C., Stoudenmire, E. M. & Wietek, A. Bose-einstein condensation in honeycomb dimer magnets and  $\text{yb}_2\text{si}_2\text{o}_7$ . *Phys. Rev. B* **107**, 205150 (2023).
- [66] Barthel, T., Schollwöck, U. & White, S. R. Spectral functions in one-dimensional quantum systems at finite temperature using the density matrix renormalization group. *Phys. Rev. B* **79**, 245101 (2009).
- [67] Bruognolo, B., Weichselbaum, A., von Delft, J. & Garst, M. Dynamic structure factor of the spin- $\frac{1}{2}$  XXZ chain in a transverse field. *Phys. Rev. B* **94**, 085136 (2016).
- [68] Paeckel, S. *et al.* Time-evolution methods for matrix-product states. *Ann. Phys.* **411**, 167998 (2019).
- [69] Keselman, A., Balents, L. & Strykh, O. A. Dynamical signatures of quasiparticle interactions in quantum spin

- chains. *Phys. Rev. Lett.* **125**, 187201 (2020).
- [70] Drescher, M., Vanderstraeten, L., Moessner, R. & Pollmann, F. Dynamical signatures of symmetry-broken and liquid phases in an  $s = \frac{1}{2}$  Heisenberg antiferromagnet on the triangular lattice. *Phys. Rev. B* **108**, L220401 (2023).
- [71] Fishman, M., White, S. R. & Stoudenmire, E. M. The ITensor Software Library for Tensor Network Calculations. *SciPost Phys. Codebases* 4 (2022).
- [72] Wu, M., Gong, S.-S., Yao, D.-X. & Wu, H.-Q. Phase diagram and magnetic excitations of  $J_1 - J_3$  Heisenberg model on the square lattice. *Phys. Rev. B* **106**, 125129 (2022).
- [73] Gu, C., Yu, S.-L. & Li, J.-X. Spin dynamics and continuum spectra of the honeycomb  $J_1 - J_2$  antiferromagnetic Heisenberg model. *Phys. Rev. B* **105**, 174403 (2022).

### Supplementary Note 1: Spin-spin correlation function of ground state

In the main text, we present the magnetization curves, entanglement entropy, and central charge as evidence supporting the existence of four distinct phases: XY-I,  $1/3$  magnetization plateau, XY-II, and ferromagnetic phases. To characterize these phases, we utilize the spin-spin correlation function of the ground state, denoted as  $\langle S_0^x S_j^x \rangle$ , as illustrated in the Supplementary Fig. 7. In the XY-I and XY-II phases, magnetic ordering is absent in the ground state, and the spin correlation functions exhibit decay according to the power laws  $\langle S_0^x S_j^x \rangle \sim j^{-\eta}$  with  $\eta_1 \simeq 0.995$  and  $\eta_2 \simeq 0.937$ . Both of these critical exponents approach the value of 1, which is consistent with the behavior observed in the  $S = 1/2$  isotropic Heisenberg chain [56]. In the  $1/3$  magnetization plateau phase, the correlation function  $\langle S_0^x S_j^x \rangle$  rapidly decays to zero as a function of distance, whereas in the ferromagnetic phase,  $\langle S_0^x S_j^x \rangle$  remains zero for all distances. Therefore, the spin-spin correlation function  $\langle S_0^x S_j^x \rangle$  serves as a valuable tool for distinguishing between the magnetically ordered phases and critical phases within this trimer spin chain subjected to a magnetic field.

### Supplementary Note 2: Spin dynamics without the magnetic field

In our previous investigation [11], we explored the spin dynamics of a trimer chain in the absence of a magnetic field using quantum Monte Carlo with subsequent numerical analytic continuation (QMC-SAC). We demonstrated that small intertrimer interactions give rise to distinct types of collective excitations associated with the internal trimer excitations. Particularly in the intermediate-energy and high-energy regimes, the presence of doublons and quartons was revealed through the QMC-SAC calculations and theoretical analysis. These findings were corroborated by the inelastic neutron scattering measurements on  $\text{Na}_2\text{Cu}_3\text{Ge}_4\text{O}_{12}$  [12], where the trimer chain is subject to the next-nearest neighbor intratrimer exchange couplings  $J_3$ , as depicted in Fig.6(a) of main text. The  $J_3$  interaction induces frustration within each trimer, which may lead to a negative sign problem in the QMC-SAC calculations. Therefore, we mainly employ the density matrix renormalization group and time-dependent variational principle (DMRG-TDVP) to investigate the spin dynamics of trimer systems under a magnetic field. Supplementary Fig. 8 presents the results of spin dynamics  $\mathcal{S}(q, \omega) = 3\mathcal{S}^{xx}(q, \omega)$  for  $g = 0.1$  obtained through the QMC-SAC, DMRG-TDVP and CPT calculations, considering the trimer chain without a magnetic field, which preserves the  $\text{SU}(2)$  symmetry. All three methods successfully reveal the low-energy continuum, as well as intermediate-energy and high-energy excitations corresponding to the spinons, doublons, and quartons, respectively. Only minor differences are present in certain spectral details. For example, the QMC-SAC calculation

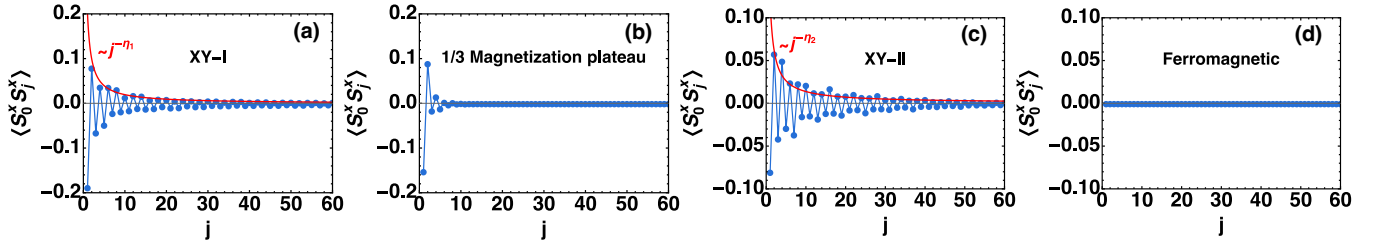


FIG. 7. Spin-spin correlation function of ground state  $\langle S_0^x S_j^x \rangle$  obtained from DMRG calculations.  $\langle S_0^x S_j^x \rangle$  as functions of distances between spins for (a) XY-I phase ( $H_z = 0.2$ ), (b) 1/3 magnetization plateau phase ( $H_z = 1.0$ ), (c) XY-II phase ( $H_z = 1.5$ ), and (d) Ferromagnetic phase ( $H_z = 2.0$ ). The red lines are the fits of correlation functions,  $\langle S_0^x S_j^x \rangle \sim j^{-\eta}$ , which indicates the correlation functions decay according to power laws with the critical exponents (a)  $\eta_1 \simeq 0.995$  and (c)  $\eta_2 \simeq 0.937$ . All results are from the case where  $g = 0.5$  and  $L = 180$ .

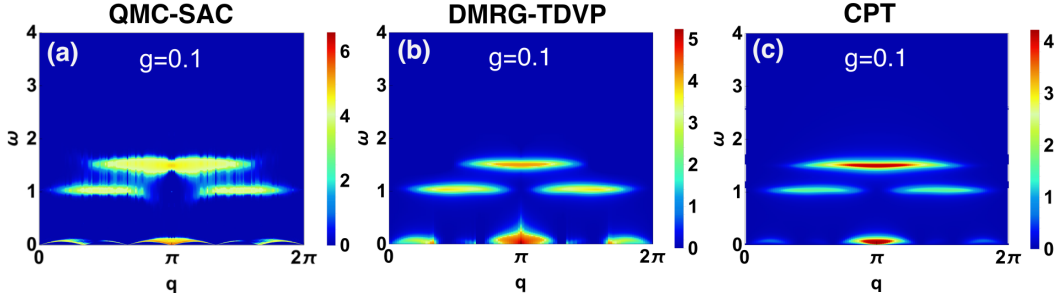


FIG. 8. Dynamic spin structure factor  $\mathcal{S}(q, \omega)$  obtained from (a) QMC-SAC, (b) DMRG-TDVP and (c) CPT calculations for the trimer chain without magnetic field. The QMC-SAC data is sourced from our previous study [11]. The color coding of  $\mathcal{S}(q, \omega)$  uses a piecewise function with the boundary value  $U_0 = 4$ . Below the boundary, the low-intensity portion is characterized by a linear mapping of the spectral function to the color bar, while above the boundary a logarithmic scale is used,  $U = U_0 + \log_{10}[\mathcal{S}(q, \omega)] - \log_{10}(U_0)$ .

effectively characterized the spinon continuum with high resolution in the low-energy regime, while the DMRG-TDVP and CPT calculations distinctly separated the doublons and quartons in the intermediate-energy and high-energy regimes. These methods offer reliable results for exploring the spin dynamics of the trimer chain.

In order to enhance the understanding of the propagation of doublons and quartons, we provide a physical elucidation in Supplementary Fig. 9. We first consider the excitation of a doublon, as depicted in Supplementary Fig. 9(a), one trimer is excited to its second-excited doublet, resulting in a flipped effective spin. This excitation is characterized by  $|\Delta M| = 1$  and the formation of two domain walls. These mobile domain walls, referred to as spinons, while not entirely free, remain tethered to the persistent central doublet. Consequently, the central doublet propagates through the system, accompanied by spinons, which gives rise to numerous internal modes within these composite excitations, thereby generating a band of finite width. Next, we examine to the quarton, which presents several possibilities for creating an excitation with  $|\Delta M| = 1$  based on the trimer excitations. For simplicity, we consider two cases involving the  $S^z = 3/2$  states to illustrate the propagation of quartons with and without domain walls. In Supplementary Fig. 9(b), an effective spin  $S^z = -1/2$  is replaced by the

$S^z = 3/2$  state, then an excitation  $|\Delta M| = 2$  is generated. To achieve the excitation  $|\Delta M| = 1$ , it is necessary to flip one of the neighboring  $S^z = 1/2$  spins downward, which creates a domain wall. Additionally, on the opposite side of the excited trimer, a domain wall may also propagate outward. Thus, the central excited state propagates throughout the system, enveloped by two domain walls. In Supplementary Fig. 9(c), the replacement of an effective spin  $S^z = 1/2$  with the  $S^z = 3/2$  state leads to the presence of two domain walls, which subsequently disappear during the propagation of the central excited state. Then a quarton propagates without domain walls. If we restore spin-rotation symmetry and explore alternative scenarios, quartons can emerge through analogous mechanisms. For further insights into the dynamics of doublons and quartons, we refer the interested reader to the Ref. [11].

### Supplementary Note 3: Longitudinal excitation spectrum

Let us examine the longitudinal excitation spectrum  $\mathcal{S}^{zz}(q, \omega)$  at  $g = 0.8$  for the XY-I phase, the 1/3 magnetic plateau phase, and the XY-II phase. As shown in Supplementary Fig. 10, the excitations in two XY phases are gapless, whereas they are gapped in the 1/3 magnetic plateau phase. In the ferromagnetic phase, where



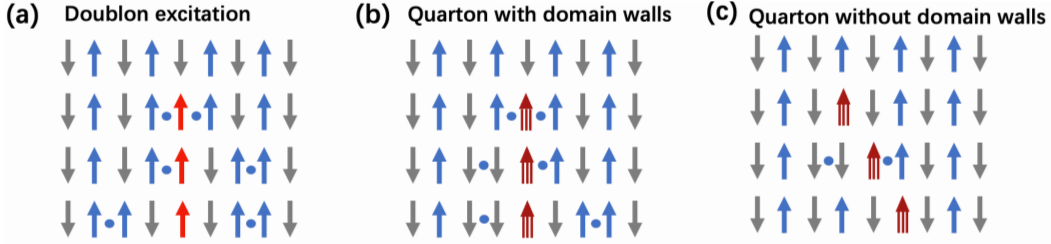


FIG. 9. **Schematic representation of propagating doublon and quarton.** The excitation mechanism and propagation of a quasiparticle are illustrated from top to bottom. Each arrow represents an effective spin of one trimer. (a) A doublon excitation, in which the spinons (domain walls indicated by dots) are bound to one excited trimer indicated by the red color. (b)(c) Quartons with and without domain walls for  $\Delta M = 1$ . The dark red arrow represents the second excited state of single trimer with  $S^z = 3/2$ .

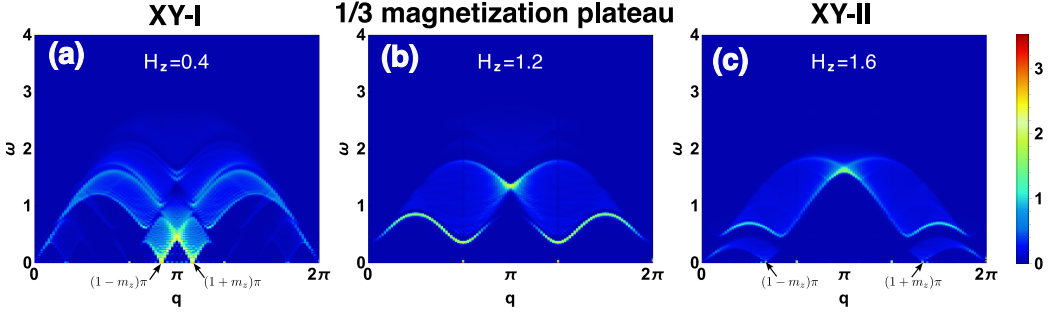


FIG. 10. **Dynamic spin structure factor  $\mathcal{S}^{zz}(q, \omega)$  obtained from DMRG-TDVP calculations for different phases.**  $\mathcal{S}^{zz}(q, \omega)$  in (a) XY-I phase, (b) 1/3 magnetization plateau phase, and (c) XY-II phase. All results are from the case where  $g = 0.8$  and  $L = 120$ . The color coding of  $\mathcal{S}^{zz}(q, \omega)$  uses a piecewise function with the boundary value  $U_0 = 2$ . Below the boundary, the low-intensity portion is characterized by a linear mapping of the spectral function to the color bar, while above the boundary a logarithmic scale is used,  $U = U_0 + \log_{10}[\mathcal{S}^{zz}(q, \omega)] - \log_{10}(U_0)$ .

all spins are polarized in the  $z$  direction, the longitudinal excitation spectrum is nonexistent. In both the XY-I and XY-II phases, the intraband zero-energy excitations correspond to the longitudinal fluctuations in the framework of spinless fermion [57]. The incommensurability observed in the spin dynamics is evidenced by the splitting of the excitation bands. In the XY-I phase, see Supplementary Fig. 10(a), the longitudinal excitations preserve the total particle number without altering the magnetization of the ground state, which indicates that the incommensurate fluctuations approaching zero energy at  $q = (1 \pm m_z)\pi$  with  $m_z = 0.1111$  being the magnetization normalized by its saturation value. In the XY-II phase, see Supplementary Fig. 10(c), the incommensurate fluctuations attain a zero energy state at  $q = (1 \pm m_z)\pi$  where  $m_z = 0.5697$ .

#### Supplementary Note 4: Effects of intertrimer interaction on the spin dynamics

In the main text, we have discussed the effects of a magnetic field on the spin dynamics by considering a fixed value of  $g$ , how the spectra evolve with varying  $g$  will provide further insights into the spin dynamics of the trimer chain under the influence of a magnetic field. Sup-

plementary Fig. 11 presents the  $\mathcal{S}^{xx}(q, \omega)$  for four distinct phases as  $g$  is varied. Within the XY-I phase, as illustrated in Supplementary Fig. 11 (a1)-(a5), the spectra remain gapless. A low value of  $g$  induces the clear separation of spectra corresponding to different energy levels, which includes the presence of doublons, upper quartons, and lower quartons, as discussed in the main text. As  $g$  increases, the intermediate-energy and high-energy spectra gradually merge, and eventually forming a continuum with the low-energy spectrum. When  $g = 1$ , the trimer chain becomes the Heisenberg XXX model, a little magnetic field ( $H_z = 0.1$ ) induces an incommensurate order leading to a slight shift at the lower boundary of the two-spinon continuum. In the 1/3 magnetization plateau phase, the gap at  $q = \pi$  diminishes with as  $g$  increases. The low-energy reduced spin wave, intermediate-energy doublons, and high-energy quartons gradually lose their identity and merge as  $g$  approaches 1. Gapless excitations and the merging of spectra are also observed in the XY-II phase, but there are some distinctions compared to the XY-I phase. For example, when  $g = 0.2$ , a new energy band emerges near  $\omega = 1$  that has no trail in other three phases. In the ferromagnetic phase, the gap at  $q = \pi$  decreases with increasing  $g$ . The excitation

spectra continue to be characterized by the spin waves, but exhibit two energy levels for the same wave vector at the edges of the Brillouin zone due to the periodic potential arising from the trimerized interaction. When  $g = 1$ , the system restores the translational invariance, and its excitation spectrum becomes a single one described by a cosine function of momentum.

### Supplementary Note 5: Exact diagonalization results

In addition to the DMRG-TDVP and CPT calculations, we have also applied the exact diagonalization (ED) method to study the spin dynamics. The ED method serves as a fundamental and straightforward approach for calculating the eigenenergies and eigenstates of a spin models with small sizes, which is essential for analyzing quantum phase transitions and magnetic excitations in spin systems. In the main text, the quantum critical points of Fig.2(b) and all results presented in Fig.(4) are derived from the ED calculations. Initially, we perform ED calculations to obtain reliable results for further investigation, as these calculations are computationally efficient and require minimal resources. When addressing larger system sizes, we employ symmetries to block diagonalize the Hamiltonian, thereby reducing computational time and memory usage. Nevertheless, the finite-size effects remain significant. To gain more reliable insights into the thermodynamic limit, we employ advanced numerical methods, such as quantum Monte Carlo, DMRG and CPT. By comparing the results obtained from these various methods, we can draw more credible conclusions.

In Supplementary Fig. 12, the longitudinal spin excitations  $\mathcal{S}^{zz}(q, \omega)$  of the XY-I, 1/3 magnetization plateau, and XY-II phases are present. These findings are in excellent agreement with those presented in Supplementary Fig.10, particularly with respect to the incommensurate wave numbers at zero energy and the characteristics of excitation spectra for the three phases. Furthermore, Supplementary Fig. 13 and Fig. 14 display the results of  $\mathcal{S}^{xx}(q, \omega)$  for different phases, which are consistent with the results presented in Figs.(2) and (3) of the main text, respectively.

### Supplementary Note 6: Dispersion relations

In the main text, the dispersion relations provide valuable insights into the excitation mechanisms underlying various spin dynamics. When  $g$  is small, the intermediate-energy and high-energy excitations are primarily localized within the trimers. To confirm the nature of these quasiparticles across different phases, we propose a methodology for deriving their dispersion relations through the imitation of complex ground states. These dispersion relations are consistent with the DMRG-TDVP and CPT results on the location and band widths of excitations spectra (see Fig.3(e) and Fig.5 of main text), indicating that our understanding of the

excitation remains accurate, despite the utilization of a highly simplified approximation for the ground state in our calculations.

Here, we delineate the primary procedures for deriving the dispersion relations. In the absence of a magnetic field, the trimer chain can be effectively described by an antiferromagnetic Heisenberg model, where the effective interaction is contingent upon the intertrimer interaction  $J_{\text{eff}} = 4J_2/9$  [11]. Given the weak intertrimer interaction and the doubly degenerate ground state, each trimer can be represented as an effective spin  $S = 1/2$ . Therefore, the assumption that the ground-state wave function of spin chain is a product state of ground states of each trimer provides a viable approach to simulate the internal trimer excitations. Upon the introduction of a magnetic field, as discussed in the main text, a quantum phase transition presents, resulting in gapless or gapped ground states in different phases. Our findings indicate that this assumption remains applicable for analyzing excitations in the XY-I and the 1/3 magnetization plateau phases. In the XY-I phase, we assume that the ground-state wave function of the trimer chain is a product state of  $|0\rangle$  and  $|1\rangle$ ,

$$|\psi\rangle_{\text{g}} = |0\rangle_1 |1\rangle_2 \cdots |0\rangle_{N-1} |1\rangle_N, \quad (29)$$

where  $|0\rangle$  and  $|1\rangle$  is the ground state and first excited state of a single trimer, respectively, as shown in Fig.(4) of main text. We disregard interactions and instead focus on  $2^{N-1}$  degenerate ground states, while imposing the constraint on the magnetic quantum numbers  $\sum M_i = 0$ . Even if the magnetic field induces an incommensurate ground state with minimal magnetization, the aforementioned assumption continues to hold. It is important to emphasize that our objective is to investigate excitations above the  $2^N$ -fold degenerate ground-state manifold, rather than employing degenerate perturbation theory. In this study, we do not engage in a formal perturbation expansion; rather, we opt to construct intuitive variational states that encompass the internal excitations of a single trimer.

For the intermediate-energy excitations, we choose the  $r$ th trimer to be excited from  $|0\rangle$  to  $|3\rangle$  with  $\Delta M = -1$  or from  $|1\rangle$  to  $|2\rangle$  with  $\Delta M = 1$ . The corresponding excited wave function is then given by

$$|\psi\rangle_{\text{e}}^r = |0\rangle_1 |1\rangle_2 \cdots |3\rangle_r \cdots |0\rangle_{N-1} |1\rangle_N. \quad (30)$$

To impart momentum to this excitation, we perform a Fourier transformation on the excited state, resulting in

$$|\psi\rangle_{\text{e}}^q = \frac{1}{\sqrt{N}} \sum_{r=1}^N e^{-iqr} |\psi\rangle_{\text{e}}^r. \quad (31)$$

Next, we proceed to calculate the expectation values of the Hamiltonian in both the ground state and the first excited trimer momentum state to derive the dispersion

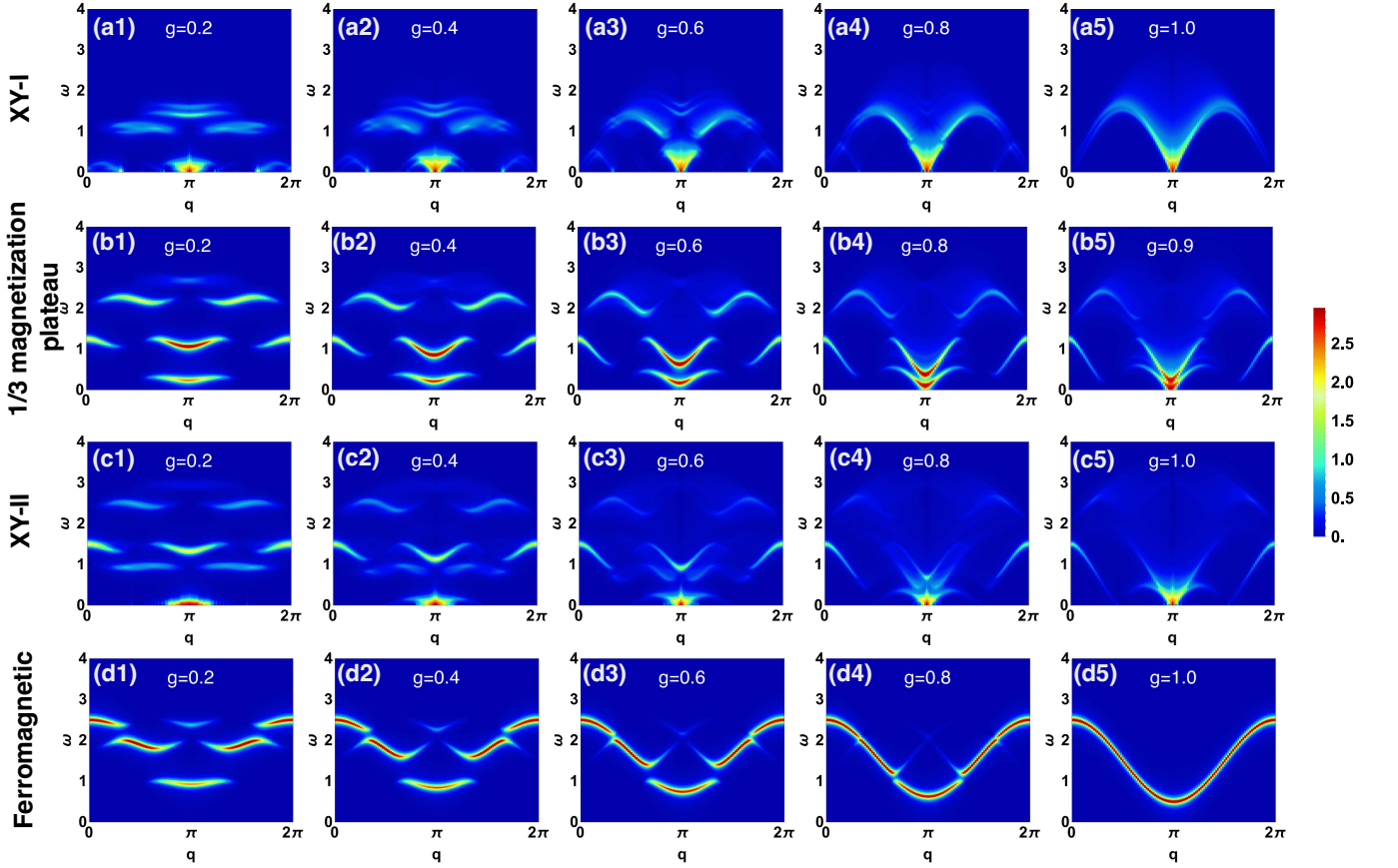


FIG. 11.  $S^{xx}(q, \omega)$  obtained from DMRG-TDVP calculations for different phases.  $S^{xx}(q, \omega)$  in (a1)-(a5) XY-I phase ( $H_z = 0.1$ ), (b1)-(b5) 1/3 magnetization plateau phase ( $H_z = 1.25$ ), (c1)-(c5) XY-II phase, and (d1)-(d5) ferromagnetic phase ( $H_z = 2.0$ ) for different intertrimer interaction  $g$ . All results are from the case where  $L = 120$ . Particularly, we choose  $g = 0.9$  in (b5) for the reason that  $H_z = 1.25, g = 1.0$  is a critical point. The color coding of  $S^{xx}(q, \omega)$  uses a piecewise function with the boundary value  $U_0 = 2$ .

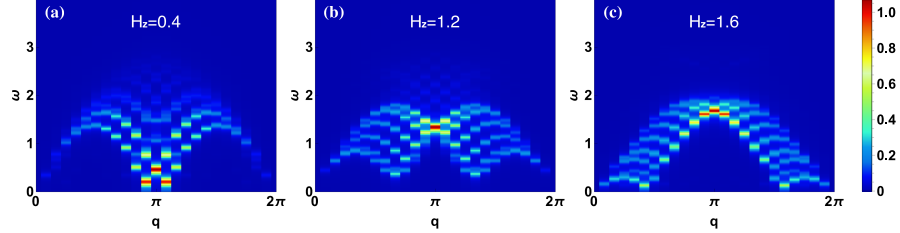


FIG. 12.  $S^{zz}(q, \omega)$  obtained from ED calculations for different phases.  $S^{zz}(q, \omega)$  in (a) XY-I phase, (b) 1/3 magnetization plateau phase, and (c) XY-II phase. All results are from the case where  $g = 0.8$  and  $L = 24$ . The color coding of  $S^{zz}(q, \omega)$  uses a piecewise function with the boundary value  $U_0 = 0.2$ .

relations associated with the intermediate-energy excitations within the reduced Hilbert space,

$$\begin{aligned} \epsilon(q) &= \langle H \rangle_e - \langle H \rangle_g \\ &= \frac{q}{e} \langle \psi | H | \psi \rangle_e^q - \frac{q}{g} \langle \psi | H | \psi \rangle_g^q. \end{aligned} \quad (32)$$

Thus, the dispersion relations corresponding to the

intermediate-energy doublon are given by,

$$\epsilon_D^{\text{red}}(q) = \begin{cases} -\frac{1}{3}g \cos q + \mathbb{E}_1 - \mathbb{E}_0 + H_z - \frac{1}{9}g, \\ -\frac{2}{9}g \cos q + \mathbb{E}_1 - \mathbb{E}_0 + H_z, \\ -\frac{2}{9}g \cos q + \mathbb{E}_1 - \mathbb{E}_0 + H_z + \frac{2}{9}g, \\ -\frac{2}{9}g \cos q + \mathbb{E}_1 - \mathbb{E}_0 + H_z + \frac{2}{9}g, \end{cases} \quad (33)$$

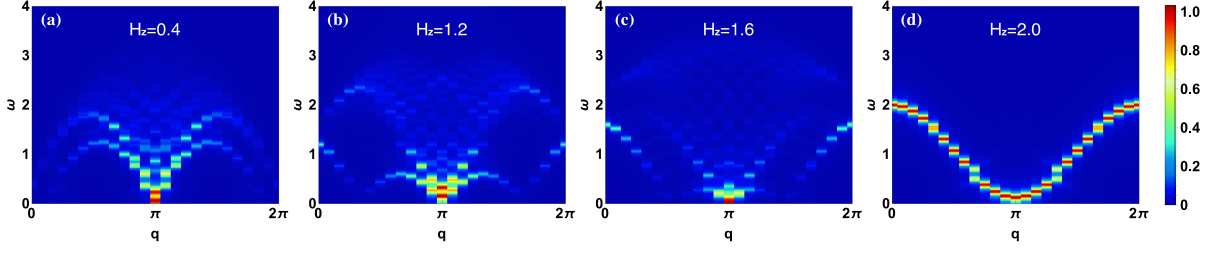


FIG. 13.  $S^{xx}(q, \omega)$  obtained from ED calculations for different phases.  $S^{xx}(q, \omega)$  in (a) XY-I phase, (b) 1/3 magnetization plateau phase, (c) XY-II phase, and (d) Ferromagnetic phase. All results are from the case where  $g = 0.8$  and  $L = 24$ . The color coding of  $S^{xx}(q, \omega)$  uses a piecewise function with the boundary value  $U_0 = 0.2$ .

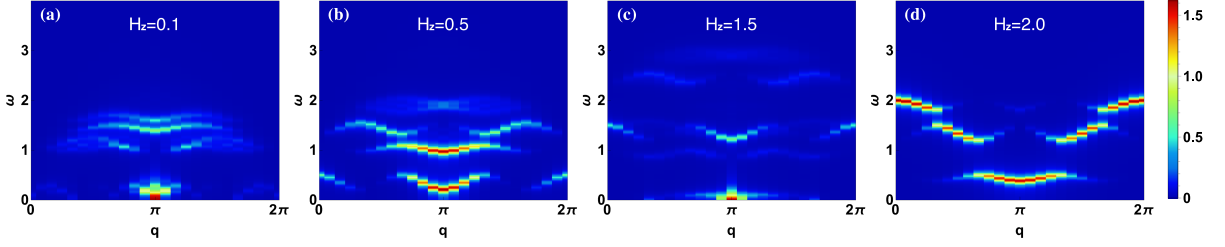


FIG. 14.  $S^{xx}(q, \omega)$  obtained from CPT and DMRG-TDVP calculations for different phases with weak inter-trimer interaction.  $S^{xx}(q, \omega)$  in (a) XY-I phase, (b) 1/3 magnetization plateau phase, (c) XY-II phase, and (d) Ferromagnetic phase. All results are from the case where  $g = 0.3$  and  $L = 24$ . The color coding of  $S^{xx}(q, \omega)$  uses a piecewise function with the boundary value  $U_0 = 0.2$ .

which are independent of the length of the spin chain.  $\mathbb{E}_0$  and  $\mathbb{E}_1$  are the ground-state and first excited-state energies of one single trimer in the absence of magnetic field, respectively. By substituting  $q$  with  $3q$ , we can derive the unfolded dispersion relations across the entire Brillouin zone, as shown in Eq.(11) of main text. To illustrate the computational process, we present Supplementary Fig. 15, which demonstrates that only 4 trimers are necessary to obtain all the dispersion relations. For the high-energy excitations, the  $r$ -th trimer is excited from  $|0\rangle$  to  $|4\rangle$  with  $\Delta M = 1$  or from  $|0\rangle$  to  $|6\rangle$  with  $\Delta M = -1$ . Similar calculations can be performed to obtain the dispersion relations of the high-energy modes. However, the magnetic field results in the splitting of the high-energy spectra into two branches, attributable to the varying spin quantum numbers  $\Delta M = \pm 1$ . These branches are referred to as the upper quarton and lower quarton (see Eq.(12) and Eq.(13) of main text), respectively.

In the 1/3 magnetization plateau phase, the gapped ground state facilitates the calculations. As depicted in Supplementary Fig. 15(b), the ground state is con-

structed from a product of polarized trimers (as the effective spins  $S_{\text{eff}} = 1/2$ ). The low-energy excitation arise from the flipping of an effective spin, akin to the formation of spin wave, but within a reduced Hilbert space. Therefore, the excitation from  $|0\rangle$  to  $|1\rangle$  with  $\Delta M = -1$  is characterized by the reduced spin wave.

Additional excitations also emerge from the internal trimer excitations, such as  $|0\rangle \rightarrow |3\rangle$  with  $\Delta M = -1$ ,  $|0\rangle \rightarrow |4\rangle$  with  $\Delta M = 1$ , and  $|0\rangle \rightarrow |6\rangle$  with  $\Delta M = -1$ . Each excitation possesses a singular dispersion relation that aligns well with the excitation spectrum. In the high-energy regime, the presence of a continuum with weak intensity may originate from the fractional spinons, as discussed in our previous study [11]. Furthermore, in Supplementary Fig. 16, the gap between the ground state and the first excited state provides effective protection for the aforementioned excitations. Even when the intertrimer interaction increases to  $g = 0.8$ , the dispersion relations continue to effectively capture the internal trimer excitations. An increase in the intertrimer interaction  $g$  leads to the merging of these excitation spectra, leading to the formation of a continuum.

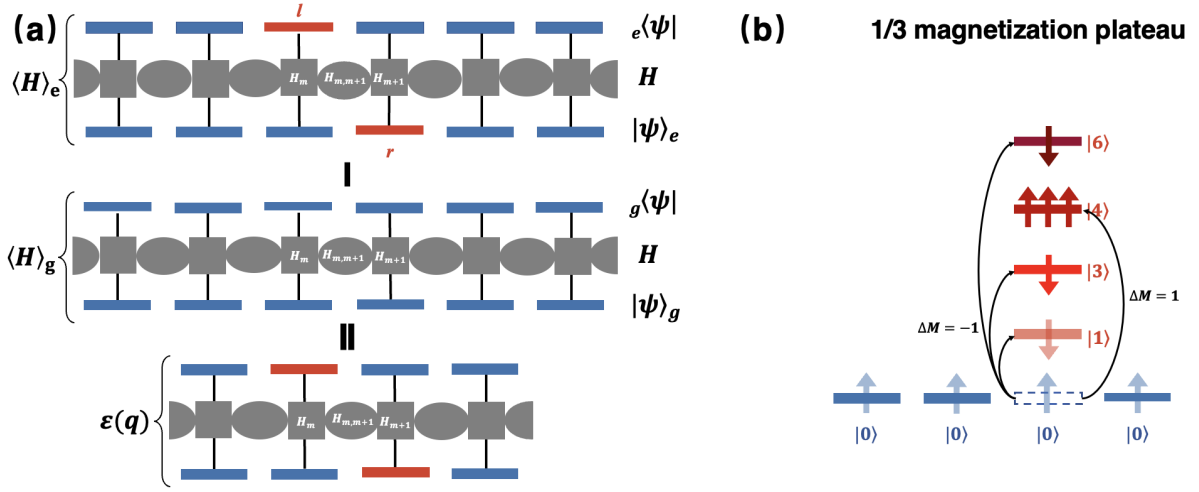


FIG. 15. **Graphical representation of the calculation of the dispersion relation  $\epsilon(q) = \langle H \rangle_e - \langle H \rangle_g$ .** (a) The trimer eigenstates are shown as darker blue (ground states) and red (excited states). With these states, the excitations with  $|\Delta M| = 1$  originate from a trimer ground state  $|0\rangle_r^1$  on the trimer located at  $r$  when excited to one of  $|1\rangle_r$ ,  $|3\rangle_r$ ,  $|4\rangle_r$ , and  $|6\rangle_r$  (and in the corresponding bra states we use the site index  $l$  instead of  $r$ ). The excitations are given momentum  $q$ , and the matrix elements contributing to the dispersion relation are indicated. (b) The construction of ground state and excitation mechanism in the 1/3 magnetization plateau phase.

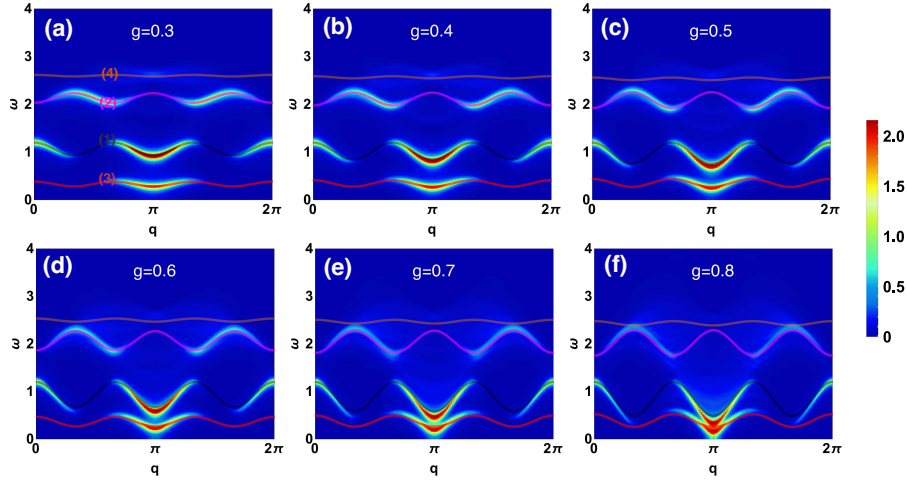


FIG. 16.  $S^{xx}(q, \omega)$  in 1/3 magnetization plateau phase for different  $g$ . All results are obtained by DMRG-TDVP calculations for  $L = 120$ ,  $H_z = 1.2$ , and the color coding of  $S^{xx}(q, \omega)$  uses a piecewise function with the boundary value  $U_0 = 2$ . The dispersion lines with colors and numbers are corresponding to the different localized excitations in a single trimer. (1)(2)(4) are the excitations from  $|0\rangle \rightarrow |1\rangle$ ,  $|0\rangle \rightarrow |3\rangle$  and  $|0\rangle \rightarrow |6\rangle$  with  $\Delta M = -1$ , respectively. (3) is the excitations from  $|0\rangle \rightarrow |4\rangle$  with  $\Delta M = 1$ .